

# $\Sigma$ -net: Systematic Evaluation of Iterative Deep Neural Networks for Fast Parallel MR Image Reconstruction

Kerstin Hammernik<sup>1\*</sup>, Jo Schlemper<sup>1,2</sup>, Chen Qin<sup>1</sup>, Jimming Duan<sup>1,3</sup>, Ronald M. Summers<sup>4</sup> and Daniel Rueckert<sup>1</sup>

<sup>1</sup> Department of Computing, Imperial College London, London, United Kingdom

<sup>2</sup> Hyperfine Research Inc., Guilford, CT, USA

<sup>3</sup> School of Computer Science, University of Birmingham, Birmingham, United Kingdom

<sup>4</sup> NIH Clinical Center, MD, USA

\*Correspondence to: Kerstin Hammernik

Department of Computing  
Imperial College London  
South Kensington Campus  
London SW7 2AZ, United Kingdom  
E-mail: k.hammernik@imperial.ac.uk

Preliminary data for this manuscript were submitted to the fastMRI challenge (team *holykspace*) and to ISMRM 2020.

Grant Sponsor: The work was funded in part by the EPSRC Programme Grant (EP/P001009/1) and by the Intramural Research Programs of the National Institutes of Health Clinical Center (1Z01 CL040004).

Running Title:  $\Sigma$ -net: Systematic Evaluation of Iterative Deep Neural Networks for Fast Parallel MR Image Reconstruction

Number of Words (Abstract): 206

Number of Words (Body): Approx. 5000

Number of Figures and Tables: 8

Number of Citations: 89

Number of Supporting Material (Figures / Videos / Tables): 4

**Submitted to Magnetic Resonance in Medicine**

## ABSTRACT

**Purpose** To systematically investigate the influence of various data consistency layers, (semi-)supervised learning and ensembling strategies, defined in a  $\Sigma$ -net, for accelerated parallel MR image reconstruction using deep learning.

**Theory and Methods** MR image reconstruction is formulated as learned unrolled optimization scheme with a Down-Up network as regularization and varying data consistency layers. The different architectures are split into sensitivity networks, which rely on explicit coil sensitivity maps, and parallel coil networks, which learn the combination of coils implicitly. Different content and adversarial losses, a semi-supervised fine-tuning scheme and model ensembling are investigated.

**Results** Evaluated on the fastMRI multicoil validation set, architectures involving raw  $k$ -space data outperform image enhancement methods significantly. Semi-supervised fine-tuning adapts to new  $k$ -space data and provides, together with reconstructions based on adversarial training, the visually most appealing results although quantitative quality metrics are reduced. The  $\Sigma$ -net ensembles the benefits from different models and achieves similar scores compared to the single state-of-the-art approaches.

**Conclusion** This work provides an open-source framework to perform a systematic wide-range comparison of state-of-the-art reconstruction approaches for parallel MR image reconstruction on the fastMRI knee dataset and explores the importance of data consistency. A suitable trade-off between perceptual image quality and quantitative scores are achieved with the ensembled  $\Sigma$ -net.

**Key words:** Parallel Imaging, Iterative Image Reconstruction, Deep Learning, Down-Up Networks, Data Consistency, Ensembling

## INTRODUCTION

Parallel Imaging (PI) (1–4) forms the foundation of accelerating data acquisition in Magnetic Resonance Imaging (MRI), which is tremendously time-consuming. In the last decade, PI combined with Compressed Sensing (CS) techniques have resulted in substantial improvements in acquisition speed and image quality (5–12) and many advanced regularization techniques have been proposed (13–15). Although PI-CS can achieve state-of-the-art performance, designing effective regularization schemes and tuning of hyper-parameters are non-trivial. Starting in 2016, deep learning algorithms have become extremely popular and effective tools in data-driven learning of inverse problems and have enabled progress beyond the limitations of CS (16–21).

Current research of deep learning for (parallel) MRI reconstruction focuses on two major branches. The first branch deals with the design of effective network architectures and loss functions. To this end, many different architectures were proposed, exploiting different content losses such as the  $\ell_1$  norm and Structural Similarity Index (SSIM) (22,23) and adversarial losses based on Generative Adversarial Networks (GANs) (24–28). The second branch deals with the question of how we can incorporate the rich domain knowledge of MRI in the reconstruction models. Various types of domain knowledge have been explored and many authors have exploited Data Consistency (DC), unique to singlecoil and multicoil imaging, iterative reconstruction approaches (16, 28–31),  $k$ -space learning (32–35), complex geometry (36, 37) and dedicated applications such as multi-contrast reconstruction (38,39), dynamic MRI (40–45) and Magnetic Resonance (MR) fingerprinting (36, 46). For further references in this field, we refer the interested reader to survey papers (47–50).

Despite the tremendous volume of research, there remain several challenges in the field of learning MR image reconstruction. Learning-based approaches are often evaluated in dedicated research settings with small, homogeneous datasets, which are often not available to the public. Hence, it is often non-trivial to draw reliable conclusions from the reported findings because the results highly depend on the dataset and hyper-parameter tuning, which make many results non-reproducible. As such, it is still largely unclear which types of approaches are more effective and if they are effective in general or only effective for the application studied for a specific experimental environment.

The fastMRI knee dataset (51) is the first publicly available dataset that mitigates the issue of small, homogeneous datasets for MR image reconstruction, and was already used for evaluation in (34, 52–55). The fastMRI knee dataset consists of almost 1,500 clinical knee datasets from various Siemens MR scanners at different field strengths and contains fully-sampled coronal Proton Density (PD) scans

with and without Fat Saturation (FS), which can then be retrospectively undersampled. Examples of challenging and heterogeneous fastMRI datasets are illustrated in Supporting Figure 1. The fastMRI dataset is accompanied by the fastMRI challenge, which provides a great opportunity to push the limits of acquisition speed and compare a variety of approaches developed by the community on a common basis.

The evaluation of the fastMRI challenge relies on a Root-Sum-of-Squares (RSS) reconstruction of the fully-sampled  $k$ -space data. However, RSS reconstruction provides a bias towards approaches which do not depend on explicit coil sensitivity maps, which is evident when we compare the RSS and a sensitivity-combined reference image qualitatively and quantitatively, as shown in Supporting Figure 2. The bias is due to the fact that the RSS combination of the individual coil channels accumulates the magnitude components of the noise, which causes a bias in low signal intensity regions and in the background. Additionally, the noise does not remain Gaussian any more as the magnitude of the noise adds up in the final image, which is not the case if the images are combined with explicit coil sensitivity maps. This forces the network to learn the scan-specific noise bias, which is undesirable. Therefore, in this work, we consider sensitivity-combined reconstruction as a ground truth to appropriately evaluate the efficacy of multicoil approaches that might involve explicit coil sensitivity maps. Note that pre-whitening (56, 57) of the data might reduce this bias effect in the RSS reconstruction and also in the sensitivity-combined reconstruction, as both the noise influence of possibly broken coil elements as well as correlations between coil elements might be compensated.

The aim of this work is to bridge the gap of aforementioned challenges that we have observed in deep learning for parallel MR image reconstruction. First, we introduce the concept of Sensitivity Networks (SNs), relying on explicit coil sensitivity maps, and Parallel Coil Networks (PCNs), that learn sensitivity maps implicitly. Second, we perform a large-scale evaluation of different networks with varying DC layers and a common Down-Up Network (DUN) as regularization, which allows us to directly compare image enhancement and image reconstruction approaches with the same model capacity. Third, we study the influence of supervised learning, including both content and adversarial losses, semi-supervised fine-tuning and model ensembling, defined as  $\Sigma$ -net. These three concepts represent amongst others many state-of-the-art approaches including (16, 20, 28, 29, 51, 58–61), enabling a systematic comparisons. All experiments are performed on the fastMRI multicoil knee dataset (51), where a fully-sampled sensitivity-combined reconstruction is used as a re-defined reference for the dataset, which we denote as SENSE target throughout our manuscript. A first evaluation of  $\Sigma$ -net on the RSS references was targeted

in our fastMRI challenge submission (62) with our team *holykspace*, where  $\Sigma$ -net is among the top three performing methods on the fastMRI multicoil test and challenge dataset.

## THEORY

### Learning Unrolled Optimization

Accelerated MR image reconstruction aims at recovering a reconstruction  $x \in \mathbb{C}^{N_x}$  from a set of undersampled  $k$ -space measurements  $y \in \mathbb{C}^{N_y}$  which are corrupted by additive Gaussian noise  $n \in \mathbb{C}^{N_y}$  following

$$y = Ax + n. \quad [1]$$

This inverse problem involves a linear forward operator  $A : \mathbb{C}^{N_x} \rightarrow \mathbb{C}^{N_y}$  modelling the MR physics. Here,  $N_x$  and  $N_y$  define the dimensions of the reconstruction  $x$  and the  $k$ -space data  $y$  according to the underlying multicoil or singlecoil problem. These dimensions and the linear forward operators will be specified separately in the later sections for SNs and PCNs.

An approximate solution to the inverse problem in Equation [1] can be obtained by learning a fixed iterative reconstruction scheme (16, 29, 40, 41, 61). We define the fixed unrolled algorithm for MR image reconstruction as

$$x^{t+\frac{1}{2}} = x^t - f_{\theta^t}(x^t), \quad [2]$$

$$x^{t+1} = g(x^{t+\frac{1}{2}}, y, A) \quad [3]$$

for  $0 \leq t < T$ . Here,  $f_\theta$  represents a Neural Network (NN)-based reconstruction block with trainable parameters  $\theta$ ,  $g$  denotes a DC layer and  $T$  is the number of fixed iterations, also termed cascades (41) or stages (16) in literature. The reconstruction block in  $f_\theta$  has the form of an encoding-decoding structure, which can be realized by any type of Convolutional Neural Networks (CNNs), U-net architectures (63) or is motivated by variational methods (16). In this work, we show the efficiency of a DUN (64) over U-net for MR image reconstruction. The DC can be realized in various ways, similar to choosing an optimizer for solving inverse problems. In this work, we compare Gradient Descent (GD) (16), Proximal Gradient (PG) (29, 41) and Variable Splitting (VS) (61) schemes. Both DUNs and DC will be presented in the following sections.

## Down-Up Networks (DUNs)

Down-Up Networks (DUNs) (64) have shown many advantages compared to U-net, which will be shortly outlined, and they have also achieved top performances in the NTIRE 2019 challenge on real image denoising (65). The DUN as shown in Figure 1 first downsamples the image by convolutions with stride 2 and then performs analysis on a coarser scale. The method then applies multiple Down-Up Blocks (DUBs), similar to a U-net but with improved residual connections. The outputs of the DUBs are concatenated and further analyzed by a residual convolution/activation block, followed by sub-pixel convolutions (66). Several things can be noted: First, DUNs are more memory efficient than conventional networks because the DUN performs the bulk of the computations on a coarser scale (64). This finding was supported by comparing the memory footprint on the Graphics Processing Unit (GPU) of U-net and DUN with the same model capacity and number of base features  $n_f=64$ . We observe that the DUN only requires 72% of GPU memory compared to U-net. Note that shifting the computation to a coarser scale has not shown any limitation on analysis at the finest scale (64, 67). In fact, the DUN allows one to increase the number of features at coarse levels, which improves the expressiveness of the model. Second, the iterative down-up structures have shown to be efficient in propagating information at different scales, resulting in improved performance for super-resolution tasks (68). Third, the DUN relies on sub-pixel convolution, which performs superior in terms of expressiveness and computational efficiency over upsampling convolution (69).

In our DUN, presented in Figure 1, we first perform complex-valued whitening (70) to normalize the image and perform the learning in normalized space. The complex-valued image is split into two channels, containing the real and imaginary parts. We start with an initial number of filters  $n_f=64$ , which is doubled after each downsampling and used 2 DUBs. In the upsampling path, the number of features is doubled prior to sub-pixel shuffling to preserve the number of features. Each downsampling and upsampling is performed with stride 2. Finally, the reconstruction is unnormalized using the initial normalization parameters. Note that we did not use batch-normalization as this has been shown to have unexpected aliasing for image restoration tasks (71). While in other works it is common to use dense connections (72, 73), we did not utilise these in our network either due to their high memory requirement.

## Data Consistency (DC)

Using DC, modelled by  $g$  in Equation [3], we have the possibility to impose prior knowledge about the MR acquisition process to the learning-based reconstruction scheme. Assuming Gaussian noise  $n$  in the measurement data  $y$ , the  $\ell_2$  norm is a suitable similarity measure

$$\mathcal{D}[Ax, y] = \frac{\lambda}{2} \|Ax - y\|_2^2.$$

As DC follows a regularization by a NN in image domain, the parameter  $\lambda$  balances the impact of the DC term  $\mathcal{D}[Ax, y]$ . When including prior knowledge about the acquisition process, we have various possibilities. The simplest case is to perform a gradient step (16) related to the DC term  $\mathcal{D}[Ax, y]$

$$g_{\text{GD}}(x^{t+\frac{1}{2}}) = x^{t+\frac{1}{2}} - \lambda^t A^*(Ax^{t+\frac{1}{2}} - y), \quad [4]$$

where  $A^*$  denotes the adjoint operator of  $A$ . Instead of alternating GD, we can use a PG scheme, where the DC is modelled by the proximal mapping

$$g_{\text{PG}}(x^{t+\frac{1}{2}}) = \arg \min_x \frac{1}{2} \|x - x^{t+\frac{1}{2}}\|_2^2 + \frac{\lambda}{2} \|Ax - y\|_2^2. \quad [5]$$

This is especially feasible if the proximal mapping is easy to compute and a closed-form solution exists. If no closed-form solution exists, as this is typically the case for parallel MRI involving coil sensitivity maps, the proximal mapping can be solved numerically using a conjugate gradient optimizer (29).

For inverse problems where the inverse of  $A$ , hence, the proximal mapping in Equation [5] is intractable to compute, the operations involved in  $A$  can be split using an additional variable as proposed for sensitivity-weighted parallel MRI in (61). To review VS, we first introduce the sensitivity-weighted multi-coil operator for the  $q^{\text{th}}$  coil as  $A_q = M\mathcal{F}C_q$ . The operator  $C_q : \mathbb{C}^{N_x} \rightarrow \mathbb{C}^{N_x}$  applies the  $q^{\text{th}}$  pre-computed coil sensitivity map to  $x$ , for  $q = 1, \dots, Q$ . This is followed by a Fourier Transform (FT)  $\mathcal{F} : \mathbb{C}^{N_x} \rightarrow \mathbb{C}^{N_x}$ . The operator  $M : \mathbb{C}^{N_x} \rightarrow \mathbb{C}^{N_y}$  realizes the Cartesian sampling pattern and masks out  $k$ -space lines that were not acquired. VS divides the problem defined in Equation [5] in two sub-problems by using a coil-wise splitting variable  $z_q \in \mathbb{C}^{N_x}$

$$\begin{aligned} z_q^{t+1} &= \arg \min_{z_q} \frac{\lambda}{2} \sum_{q=1}^Q \|M\mathcal{F}z_q - y_q\|_2^2 + \frac{\alpha}{2} \sum_{q=1}^Q \|z_q - C_q x^{t+\frac{1}{2}}\|_2^2 \\ g_{\text{VS}}(x^{t+\frac{1}{2}}) &= \arg \min_x \frac{\alpha}{2} \sum_{q=1}^Q \|z_q^{t+1} - C_q x\|_2^2 + \frac{\beta}{2} \|x - x^{t+\frac{1}{2}}\|_2^2, \end{aligned}$$

where  $\alpha > 0$  and  $\beta > 0$  balance the influence of the soft constraints. Solving these sub-problems yields the following closed-form solution

$$z_q^{t+1} = \mathcal{F}^{-1} \left( (\lambda M^* M + \alpha I)^{-1} \left( \alpha \mathcal{F} C_q x^{t+\frac{1}{2}} + \lambda M^* y_q \right) \right)$$

$$g_{\text{VS}}(x^{t+\frac{1}{2}}) = \left( \beta I + \alpha \sum_{q=1}^Q C_q^* C_q \right)^{-1} \left( \beta x^{t+\frac{1}{2}} + \alpha \sum_{q=1}^Q C_q^* z_q^{t+1} \right).$$

Here,  $I$  denotes the identity matrix and  $*$  the adjoint operation.

All presented DC layers, i.e., GD, PG and VS ensure soft DC to the measurement data  $y$ , representing image reconstruction networks. By setting  $\lambda=0$  in Equation [4] we obtain

$$g_{\text{ID}}(x^{t+\frac{1}{2}}) = x^{t+\frac{1}{2}}.$$

This represents an image enhancement network, where the influence of DC is omitted.

## Sensitivity Networks and Parallel Coil Networks

We investigate two types of architectures for parallel MR image reconstruction: Sensitivity Networks (SNs) and Parallel Coil Networks (PCNs), visualized in Figure 2. The major difference between these network architectures is their way of (weighted) coil combination.

For SNs, the coil combination is defined with the operator  $A : \mathbb{C}^{N_x} \rightarrow \mathbb{C}^{N_y}$  using explicit coil sensitivity maps as in (16). To overcome Field of View (FoV) issues in the SNs, we use an extended set of  $M=2$  coil sensitivity maps according to (4), hence, reconstructing  $x = [x_1, x_2]$ . The dimensions are given as  $N_x = N_{\text{FE}} \cdot N_{\text{PE}} \cdot M$  and  $N_y = N_{\text{FE}} \cdot N_{\text{PE}} \cdot Q$ , where  $N_{\text{FE}}$  and  $N_{\text{PE}}$  denote the number of Frequency Encoding (FE) and Phase Encoding (PE) lines, respectively. In the case of SNs, the NN  $f_\theta : \mathbb{C}^{N_x} \rightarrow \mathbb{C}^{N_x}$  has two complex-valued input and output channels.

In contrast, PCNs reconstruct individual coil images  $x = [x_1, \dots, x_Q]$  for  $Q$  coils, hence,  $N_x = N_y = N_{\text{FE}} \cdot N_{\text{PE}} \cdot Q$ . The operator  $A : \mathbb{C}^{N_x} \rightarrow \mathbb{C}^{N_y}$  simply performs coil-wise FTs and  $k$ -space masking and results in the same DC term as in (41) for single-coil MR imaging. The NN  $f_\theta : \mathbb{C}^{N_x} \rightarrow \mathbb{C}^{N_x}$  of PCNs has  $Q$  complex-valued input and output channels and learns weighted coil combination implicitly.

For both SNs and PCNs, the final reconstruction  $x_{\text{rec}}$  is obtained by a RSS combination of the individual network output channels of  $x^T$ . The NN is realized using a DUN (64) as described in the previous section. For the PCN, only PG networks will be investigated as no coil sensitivity maps are involved and a closed-form solution for the proximal mapping Equation [5] exists.

## Supervised Learning

The networks were trained using a combined  $\ell_1$  and SSIM (22, 23) content loss  $\ell_{\text{base}}$  between the reference  $x_{\text{ref}}$  and the reconstruction  $x_{\text{rec}} = x^T$

$$\ell_{\text{base}}(x_{\text{rec}}, x_{\text{ref}}) = 100 - \text{SSIM\%}(m \odot |x_{\text{rec}}|, m \odot |x_{\text{ref}}|) + \gamma_{\ell_1} \ell_1(m \odot |x_{\text{rec}}|, m \odot |x_{\text{ref}}|).$$

where  $\odot$  is the pixel wise product and  $|\cdot|$  denotes the RSS reconstruction to combine the individual output channels. The SSIM% is given in percent only during training, to increase numerical stability. This loss formulation also involves a binary foreground mask  $m$  to focus the network training on the image content and not on the background. The parameter  $\gamma_{\ell_1} = 10^{-3}$  is chosen empirically to match the scale of the two losses.

In addition to the content loss  $\ell_{\text{base}}$ , we investigate the impact of an adversarial loss based on Least Squares Generative Adversarial Networks (LSGAN). Specifically, we adopt the LSGAN formulation as proposed in (74), and combine it with  $\ell_{\text{base}}$ , yielding the following two objective functions, which are optimized in an alternating manner,

$$\begin{aligned} & \min_{\eta} \frac{1}{2} \mathbb{E}_{x_{\text{ref}} \sim p_{x_{\text{ref}}}} [(h_{\eta}(m \odot |x_{\text{ref}}|) - 1)^2] + \frac{1}{2} \mathbb{E}_{x^0 \sim p_{x^0}} [(h_{\eta}(m \odot |x_{\text{rec}, \theta}|))^2] \\ & \min_{\theta} \frac{1}{2} \mathbb{E}_{x^0 \sim p_{x^0}} [(h_{\eta}(m \odot |x_{\text{rec}, \theta}|) - 1)^2] + \gamma_{\text{base}} \ell_{\text{base}}(m \odot |x_{\text{rec}, \theta}|, m \odot |x_{\text{ref}}|). \end{aligned}$$

Here,  $h_{\eta}$  defines a discriminator network with trainable parameters  $\eta$  which has the task to identify if the input is a fully-sampled image  $x_{\text{ref}}$  or the generated reconstruction image  $x_{\text{rec}, \theta}$ . Note that we add  $\theta$  in the subscript here to clarify the dependency on trainable parameters  $\theta$  of the reconstruction network. Furthermore,  $p_{x_{\text{ref}}}$  and  $p_{x^0}$  are distributions over reference data  $x_{\text{ref}}$  and undersampled zero-filling reconstructions  $x^0$ , respectively. Here,  $x^0$  serves as initialization of the reconstruction network to generate  $x_{\text{rec}, \theta} = x^T$ . For the discriminator, we used the same architecture as for the super-resolution GAN proposed in (75). The hyper-parameter  $\gamma_{\text{base}}$  defines the trade-off between the effects of the content and adversarial losses, and is chosen as 0.1 empirically.

## Semi-Supervised Fine-Tuning

A major drawback of supervised learning approaches is their tendency to produce overly smooth reconstructions. Pixel-based losses such as the  $\ell_1$  or  $\ell_2$  norm do not have the capability to account for fine details and texture in the images and are known for their averaging behaviour (75). Even patch-based losses such as SSIM do not have the capability to adapt to the characteristics of MR images. Hence,

supervised learning produces the best reconstruction to account for a wide range of given training data from various scanners, contrasts and noise levels, according to the underlying loss function. However, if new data are presented which have different characteristics, the trained model might not produce appealing results. To overcome these issues, we propose a semi-supervised fine-tuning approach, motivated by (76, 77). We consider the problem

$$\min_{\theta} \frac{1}{2} \|Ax_{\text{rec},\theta} - y\|_2^2 + \gamma_{\text{prior}} \max(1 - \text{SSIM}\%(m \odot |x_{\text{rec},\theta}|, m \odot |x_{\text{prior}}|) - \gamma_{\text{th}}), 0)^2. \quad [6]$$

The aim is to adapt the network parameters  $\theta$  to new  $k$ -space data, ensured by the first DC term. Instead of using a latent noise vector as in (76), we already have a pre-trained reconstruction network involving available prior knowledge, which slightly needs to be adapted to the new data. Hence,  $\theta$  is initialized by the learned parameters of a supervised learning approach. To avoid overfitting to the  $k$ -space data, we add a regularization term based on the supervised model reconstruction, which we term now  $x_{\text{prior}}$ . Motivated by the fastMRI challenge guidelines where SSIM is the major evaluation metric, we allow the fine-tuned reconstructions to deviate from the initial reconstruction  $x_{\text{prior}}$  by a certain amount  $\gamma_{\text{th}} \in [0, 1]$ . The influence of the regularizer is handled by the parameter  $\gamma_{\text{prior}} > 0$ . The hyperparameters were set to  $\gamma_{\text{prior}}=1$  and  $\gamma_{\text{th}}=0.8$  empirically and might be adapted for specific applications.

## Ensembling

When training single models, we observe that the final reconstructions appear very similar at first glance. We note only subtle differences, not only in different areas in the image, but also in terms of quantitative values, which might end in a great dissatisfaction that apparently different models lead to similar results. This can be noted even when the same models are trained with different initializations, as the highly non-convex networks are trapped in different local minima. As these models make subtle, different errors in the reconstruction, it becomes challenging to select a single *best* model for a specific task. To overcome these uncertainties, the reconstruction models trained under the same conditions are ensembled by simple averaging. This increases the robustness not only quantitatively but also qualitatively (78), and was also used for ImageNet to yield top performances (79). In our work, we use model ensembling on all networks defined in a  $\Sigma$ -net to balance the trade-off between quantitative scores and qualitative image appearance.

## METHODS

### Data Processing

All our experiments were performed on the fastMRI knee dataset (51). Instead of using the RSS target of the fastMRI dataset, we re-defined the target as the sensitivity-weighted coil-combined image of the fully sampled data, which allowed us a valid comparison for any approach based on coil sensitivity maps. We estimated two sets ( $M=2$ ) of sensitivity maps according to soft SENSE (4) to account for any field-of-view issues or other obstacles in the data. The number of Auto-Calibration Lines (ACLs) needed for sensitivity map estimation varied according to the acceleration factor and was set to 30 ACLs for  $R=4$  and 15 ACLs for  $R=8$  for the training and validation set. Sensitivity maps for the test and challenge dataset were computed based on the provided number of low frequencies. These numbers were motivated by examining the number of given low frequencies in the test and challenge dataset. The data were normalized by a factor obtained from the low frequency scans by taking the median value of the 20% largest magnitude values, to account for outliers. Complex mean and complex pseudo co-variance normalization parameters for the DUN were also estimated from the low-frequency scans.

The fastMRI dataset contained patient volumes where each slice had a matrix size of  $(N_{\text{FE}} \times N_{\text{PE}})$ . The PE direction varied for the individual cases and the FE direction was constant  $N_{\text{FE}}=640$ . Including the  $Q=15$  coil channels and estimated sensitivity maps, this required 2.8 TB for the train and validation set. However, this resulted in a bottleneck for data reading itself. To overcome this bottleneck and accelerate the training, we pre-processed the individual channels of the fully-sampled data in FE direction and crop them to the central  $N_{\text{FE}}=320$  while keeping the PE the same, to not introduce new artifacts. Furthermore, data were stored as float16, which in total reduced the memory to 750 GB. Testing was performed on the original data.

As aforementioned in the section about supervised learning, we utilised the foreground information. The foreground masks for 10 subjects were semi-automatically generated by first using graph-cut algorithms (80) to obtain a rough segmentation, followed by manually applying standard image processing techniques including connected component analysis, hole-filling, binary mask dilation and erosion. These images were treated as ground truth to train a U-net for foreground segmentation. The trained network was applied to remainder of the data to obtain the reference foreground masks. The underlying U-net architecture consisted of  $n_f=32$  features with 4 downsampling levels. We note that perfect foreground masks are not neces-

sary and one might also estimate foreground masks from the coil sensitivity maps which was not investigated in this work. The estimated foreground masks will be provided upon request.

## Network Training

We established a common training scheme for all networks, using RMSProp with learning rate  $10^{-4}$  and batch size 1. We pre-trained all network architectures on both contrasts PD and FS for the acceleration factors  $R=4$  and  $R=8$  simultaneously for 40 epochs and randomly selected slices from the individual training cases. These networks were further fine-tuned for the individual contrasts and acceleration factors for 10 epochs using all available slices. To overcome the huge GPU memory consumption of the proposed networks, we further used a patch learning strategy (41) where we randomly extracted patches of size 96 in FE direction.

Similarly, networks with adversarial losses were also trained for each individual contrast and acceleration factor for 10 epochs based on the pre-trained models. Adam optimizer with a learning rate of  $10^{-4}$  was used to train the discriminator, while the settings for training the generator remained the same with the base model for a fair comparison. Fine-tuning was performed for 50 iterations using the Adam optimizer with learning rate of  $5 \times 10^{-5}$  at test time.

## Experimental Setup

We performed two sets of experiments. In the first set, we compared the influence of different DC layers. For SNs, we studied GD, PG and VS for image reconstruction and additionally used the identity (ID) to compare to image enhancement, for  $T=8$  cascades. We refer to these networks as  $\text{SN}_{\text{GD}}^8$ ,  $\text{SN}_{\text{PG}}^8$ ,  $\text{SN}_{\text{VS}}^8$  and  $\text{SN}_{\text{ID}}^8$ , where the superscript denotes the number of cascades. As a baseline, we trained a SN for a single cascade  $T=1$ , denoted as  $\text{SN}_{\text{ID}}^1$ , and a residual U-net. For PCNs, we performed experiments for PG, denoted as  $\text{PCN}_{\text{PG}}^8$ . All experiments were performed for shared parameters and varying parameters over the cascades, where the latter case increased the model complexity by the number of cascades as shown in Supporting Table 1. Models trained with shared parameters are denoted by an additional  $s$  in the superscript, e.g.,  $\text{SN}_{\text{GD}}^{8s}$ .

In the second set of experiments, we studied the influence of LSGAN, semi-supervised fine-tuning and model ensembling on the qualitative and quantitative image quality. These experiments were performed using  $\text{SN}_{\text{GD}}^8$  as a base network.

Evaluation was performed on the fastMRI multicoil validation set. For quan-

titative evaluation, we used the same evaluation procedure as in (51), including Normalized Mean Squared Error (NMSE), Peak Signal-To-Noise Ratio (PSNR) and SSIM. Additionally, we studied the differences in DC by plotting the dataterm argument  $Ax - y$  and reporting

$$\mathcal{D}\text{-NMSE} = \frac{1}{N_{\text{sl}}} \sum_{n=1}^{N_{\text{sl}}} \frac{\|A_n x_n - y_n\|_2^2}{\|y_n\|_2^2}$$

for a single case with  $N_{\text{sl}}$  slices.

Statistical tests were performed for each metric result to ensure that the difference in model performances were significant. For multi-model comparisons, we first performed Friedman test (81) to see if there was a significant difference in the result statistics. Once the difference was detected, we performed one-versus-all one-way Wilcoxon signed-rank test (82) with Bonferroni correction to ensure if the results from a particular model significantly differed, i.e., outperformed, the others.

## Reproducible Research

Especially in the era of machine learning, it becomes more and more challenging to reproduce different approaches because they rely on their own framework and datasets. With our work, we provide a unified framework for various regularization networks and DC layers, allowing for a fair comparison between the different network architectures. To support the reproducible research initiative (83) and to verify the results of this manuscript, we make all Pytorch source code available at <https://github.com/khammernik/sigmanet>. We built upon the fastMRI framework<sup>1</sup> and provide not only improved data loaders, but also an interface for regularization and DC layers, which can be easily extended. The framework also includes data processing scripts to reduce data and to estimate both foreground masks and coil sensitivity maps. To estimate the coil sensitivity maps, the BART toolbox (84) is required. All coil sensitivity maps are stored in \*.h5 along with other important variables. A detailed description of these files is provided in Appendix A.

## RESULTS

In the first set of experiments we compare the influence of different DC layers on parallel MR image reconstruction using SNs and PCNs, with shared and variable network parameters. The quantitative results are depicted in Table 1. We observe that the proposed DUN regularization  $\text{SN}_{\text{ID}}^1$  yields improved results compared to the

---

<sup>1</sup><https://github.com/facebookresearch/fastMRI>

U-net regularizer, depicted in the first two rows of the table. Furthermore, we note that quantitative results can be pushed by training a separate  $SN_{ID}^{8s}$ , which represents a deep residual NN which has the same model complexity as  $SN_{ID}^1$ . Table 1 also shows that any type of reconstruction network outperforms all image enhancement networks, i.e., residual U-net and  $SN_{ID}^*$ , substantially. For shared parameters, we note that reconstruction networks with PG as DC outperform GD and VS for both acceleration factors, while VS outperforms GD slightly only for acceleration factor  $R=8$ . For variable parameters in the cascades, we observe that GD as DC performs superior than PG and VS in all cases. Furthermore, we note that PCNs yield inferior quantitative results than SNs. All results were statistically significant with  $p \ll 10^{-5}$ .

The qualitative results for different DC layers is depicted in Figure 3 for a PDFS case and  $R=4$ . We observe that the reconstruction networks appear not only sharper than image enhancement networks, but also depict the correct anatomy of the lateral meniscus, indicated by the green arrow. There is no obvious difference between the different DC layers GD, PG and VS and also between PCNs and SNs. The result for  $SN_{PG}^{8s}$  appears slightly sharper and contains more noise than all other images. Similar observations can be made for a PD case at acceleration factor  $R=8$  as illustrated in Figure 4, where the anatomy in the lateral aspect of the knee greatly deviates, especially for the  $SN_{ID}^8$ . These deviations in anatomy are depicted in the detailed view of Figure 5. Additionally, we note for the PD case at acceleration  $R=8$  that some bright intensities in the lateral meniscus area are not visible in neither image enhancement nor the image reconstruction networks, indicated by the green arrow.

In the second set of experiments, we compare the influence of different (semi-)supervised learning strategies which were conducted on the base network  $SN_{GD}^8$ . The quantitative results for this set of experiments are reported in Table 2. Qualitative results for a PDFS case is depicted in Figure 6 along with a detailed view of areas of the medial and lateral aspect of the knee and the interchondylar notch. Quantitative values indicate that the base network  $SN_{GD}^8$  achieves the best scores, followed by the ensembled  $\Sigma$ -net<sup>8</sup>. The quantitative values for  $SN_{GD-FT}^8$  and  $SN_{GD-GAN}^8$  drop substantially for all cases. In the qualitative results, we observe that the base network  $SN_{GD}^8$  is most blurred. The texture is improved for  $SN_{GD-FT}^8$ , while  $SN_{GD-GAN}^8$  appears most textured. The ensembled  $\Sigma$ -net<sup>8</sup> combines the properties of different SNs and appears slightly more textured than the base network  $SN_{GD}^8$  with minimally decreased quantitative scores.

To support our findings in the importance of DC, we study the DC qualitatively and quantitatively for a single PDFS case at acceleration  $R=4$  for  $SN_{ID}^8$ ,  $SN_{GD}^8$ ,

$SN_{GD-FT}^8$  and  $SN_{GD-GAN}^8$  in Supporting Figure 3. We observe the same behaviour: The lowest SSIM score is achieved for  $SN_{ID}^8$  and the highest SSIM score for  $SN_{GD}^8$ . Scores for  $SN_{GD-FT}^8$  and  $SN_{GD-GAN}^8$  dropped again compared to  $SN_{GD}^8$ . The dataterm measure  $\mathcal{D}$ -NMSE indicates best DC for  $SN_{GD-FT}^8$ , followed by  $SN_{GD-GAN}^8$  and  $SN_{GD}^8$ . DC is not maintained in  $SN_{ID}^8$ , also supported by the  $k$ -space plot  $Ax - y$  of a depicted coil. Interestingly, the  $\mathcal{D}$ -NMSE is lower for  $SN_{GD-GAN}^8$  than  $SN_{GD}^8$ , however, we observe a bright spot in the center of  $k$ -space for  $SN_{GD-GAN}^8$ . We note that the improved textures and the drop in SSIM of  $SN_{GD-FT}^8$  from  $SN_{GD}^8$  is consistent with Equation [6], hence, expected.

## DISCUSSION

To the best of our knowledge, this is the first large-scale comparison of state-of-the-art approaches based on a systematic evaluation of different model configurations with the same model complexity. Our first set of experiments is concerned with comparing the effect of different DC layers. In particular,  $SN_{ID}$  represents any image enhancement networks like (51, 58, 59),  $SN_{GD}^8$  represents (16, 20),  $SN_{GD-GAN}^8$  represents (28),  $SN_{GD-PG}^{8s}$  represents MoDL (29),  $SN_{GD-VS}^8$  represents VS-net (61) and  $PCN_{PG}^8$  represents (55, 60). Note that the difference to the original approaches is that we have employed the same base architecture for the regularization network, realized by DUNs, and a fixed number of iterations ( $T=8$ ). This systematic evaluation allows us to compare the different approaches in a fairer and more informative way, while re-implementation of the original architectures would yield in different model complexities, i.e., number of parameters, regarding the regularization networks. From the results we have observed that while GD outperforms other DC types in many scenarios quantitatively, perceptually most models result in similar performance for the underlying experimental setup. Note that we have not compared with other extensions of unrolled approaches (40) but we believe that these extensions can mutually benefit all models, in exchange of higher memory consumption.

Regarding the training setting, we have used the same combination that worked robust across all scenarios to enable a fair comparison between different models in a reproducible way. We have used DUNs ( $SN_{ID}$ ) as the base architecture, which indeed outperforms U-net for 70% of memory utilization. This ensures sufficient expressibility of the model, yet the efficient memory usage is crucial to enable a certain number of cascades for the experiments. It is important to note that we expect further improved results by elaborating other network architectures, fine-

tuning the learning rate with, e.g., scheduling, and/or curriculum learning. Again, these strategies cannot be tested extensively as they may be model specific strategies that are based on empirical experience only. This is out of scope for this work. However we do not expect that the general trend will change according to our observations.

Besides different training procedures and DC layers, we also compare two different types of network architectures, SNs and PCNs. For SNs we provide explicit coil sensitivity maps and the coil combination is performed by the forward operator  $A$ , whereas PCNs have single-coil DC and the weighted coil combination is performed implicitly by the regularizing DUN. Both proposed architectures have approximately the same model complexity. The result indicate that both SNs and PCNs outperform image enhancement networks significantly. While large differences between SNs and PCNs are hard to spot in general, the quantitative results that training of SNs is facilitated by providing some additional prior knowledge through the forward operator  $A$ . The advantage of PCNs are that they do not require coil sensitivity maps.

One of the main aims of this work is to examine the benefits of image reconstruction approaches compared to image enhancement approaches. We have found that image reconstruction approaches significantly outperform image enhancement approaches ( $p \ll 10^{-5}$ ). However, we have observed that even without DC, high quantitative results can be achieved. Nevertheless, while the reconstruction results appear correct qualitatively, the anatomy appears completely different in certain areas compared to the reference, as illustrated in Figure 5, which might result in misdiagnosis. The enhancement approaches overfit severely, even if the overall result seems consistent. The reconstruction approaches have better DC, hence, anatomical consistency. However, for  $R=8$ , we see a loss in content for both models, highlighted by the green arrow in Figure 5, which may indicate the limit of acceleration in static 2D MRI reconstruction.

Our systematic experiments also study the influence of shared and variable parameters across the individual cascades. While variable parameters increase the model complexity by the number of cascades  $T$ , the same set of parameters is applied to the individual cascades in the shared setting (see Supporting Table 1). Our results support the findings of Aggarwal et al. (29), who also used shared parameters but a different regularization network. However, we have found that the gap between  $\text{SN}_{\text{GD}}^{8s}$  and  $\text{SN}_{\text{PG}}^{8s}$  is smaller compared the findings in (29) which might be due to a different network training procedure, imperfect validation set, different data set and most importantly, the high sensitivity of the trainable parameter  $\lambda$ .

For shared parameters, we also observe that the training of VS is very sensitive to parameter selection and the training parameters, resulting in decreased values for acceleration factor  $R=4$  and improved results for acceleration factor  $R=8$  compared to GD. The ambiguities in splitting methods, both PG and VS, are more obvious when examining the results for variable parameters. We clearly observe a decrease in quantitative values and DC with GD outperforms all other methods in the case of a variable parameter setting. We also observe instabilities during training the different architectures and a huge influence of the parameter  $\lambda$ . These findings also suggest that we have to carefully setup our training procedure and either keep  $\lambda$  and other hyper-parameters fixed or optimize with a different learning rate than the convolution kernels. We also find that the quantitative results further improve by having a greater model complexity, however, this also rises the question if it is really required to rise this complexity by such a large margin for a small improvement in quantitative values, or if more focus should be given on a careful evaluation of a specific application in future work.

The second set of experiments investigates the effect of adversarial loss, semi-supervised fine-tuning and model ensembling. We have observed that models trained with an adversarial loss can reconstruct images with visually better details and textures, though with a compromise of decreased quantitative values, which is consistent with preliminary findings (24–28,85,86). In addition, we note that combination of DC layers and adversarial loss is complementary and improved sharpness of the results with minimal risk of hallucination. Therefore, we have not made direct comparisons with methods such as DAGAN (24) and CycleGAN (25), as we have observed that  $\text{SN}_{\text{GD}}^8$  served as a superior base network than U-net. Nevertheless, we have not utilized other components proposed in literature such as perceptual loss,  $k$ -space loss and cycle consistency, but we expect that the addition of these elements can provide further improvements. Similarly, we use LSGAN as we find it to be stable, but other types of GANs, e.g., Wasserstein GAN (28), can be considered, even though extensive comparisons are beyond the scope of this work.

On the other hand, the semi-supervised approach fine-tunes each test image by considering the specific features and characteristics of the new unseen  $k$ -space data, while exploiting the prior knowledge learned from the supervised learning stage. Results show that the semi-supervised fine-tuning can recover more textures compared to the models trained with the supervised base loss alone, with more details that are specific to the test sample. We note that the fine-tuning process results in lower quantitative values. While this may appear counter intuitive, it is consistent with Equation [6] that data-specific information is recovered even though

it may not directly optimize the metric of interest. Our findings support that the balance between the perceptual quality and data fidelity shall be considered. This can be achieved via varying the trade-off parameters between different losses to find an optimal balance between them. However, the aim of this work is also to investigate the effects of these losses, thus we do not further investigate an optimal tuning of these parameters.

In addition, we have also proposed to ensemble models with different network structures and different training losses, resulting in the  $\Sigma$ -net. Model ensembling can be seen as a tool to remove random errors made by individual reconstructions. If the single model performances are on similar lines, this might push the quantitative values while exploiting the advantages from different models. It can be seen from our results that model ensembling achieves a balancing effect between different models, producing less smooth images compared to  $\text{SN}_{\text{GD}}^8$ , with relatively close quantitative scores. The current performance of model ensembling is limited by the diversities of available models, as most of them adopt the same network architecture and produce similar results. If more models with various similar architectures are included, we could expect an even better performance of model ensembling.

In this work, we have studied many variants for learning parallel MR image reconstruction systematically. In general, deep learning approaches have shown robust, near perfect result for  $R=4$  and also impressive results for  $R=8$ . However, while higher quantitative scores correlate with improved image quality in general, they simply cannot guarantee if local structures are accurately depicted, because the provided measures are not sensitive to this. This necessitates careful side-by-side comparisons such that the radiologist agrees on local, anatomical consistency. Moreover, metrics which are more sensitive to local consistencies might be a key ingredient to assess the algorithms quantitatively in the future.

Another concern is that the current limit of machine learning based algorithms for inverse problem is unclear. While this limit seems to be much further away than the current theoretical limit of CS, it is unclear how far the acceleration factor should be pushed. An acceleration factor of  $R=8$  might lead to mis-diagnosis, as our networks cannot recover the bright intensities in the lateral meniscus, as illustrated in Figure 5. Hence, the acceleration limit of MR data acquisition highly depends on the specific purpose and more application-specific approaches might be studied in the future, where higher acceleration can be considered (87, 88).

## CONCLUSION

In this work, we systematically studied different configurations of state-of-the-art network designs for parallel MR image reconstruction in image domain, including DUNs, U-net and different DC terms. To further enhance the image quality, we investigate adversarial losses and self-supervised fine-tuning. The final model ensembling to a  $\Sigma$ -net takes advantages of the strengths and weaknesses of the included network architectures and allows for both balanced quantitative scores and enhanced image quality. The proposed  $\Sigma$ -net of our team *holykspace* is among the top three performing methods on the fastMRI public and challenge leaderboard for multicoil reconstruction (62). In this work, we used a sensitivity-weighted coil-combination as reference, different from the RSS reference used in fastMRI challenge. This enabled us to minimize the effect of noise-induced bias and perform fairer comparisons of multicoil models.

This work provides general open-source tools for learning-based MRI reconstruction in image domain and provides an overview of various proposed algorithms in literature, along with their challenges in, e.g., network training. We emphasize that each model definitely has scope for further improvement based on careful hyper-parameter tuning, including variations in initialization, advanced (pre-)training schemes, different loss functions and learning rate scheduling. However, this is out-of-scope for this work as we highlight that all models were trained systematically in a common setting.

Up to now, we have only scratched the surface of deep learning for MR image reconstruction, we are yet to understand their generalization ability to, e.g., variations in anatomy, noise, contrast, as well as finding the failing mode (89). The fastMRI dataset is a big step towards reproducible MR image reconstruction research for studying the model performances, nevertheless, it raised new challenges. In particular, radiologists' perspective and quantitative scores did not align for local characteristics of the images, suggesting that one should direct the research in both careful network setup according to the underlying target application and finding new evaluation schemes to judge, which algorithms fulfill the target application's requirements.

## ACKNOWLEDGEMENTS

The work was funded in part by the EPSRC Programme Grant (EP/P001009/1) and by the Intramural Research Programs of the National Institutes of Health Clinical

Center (1Z01 CL040004).

## APPENDIX A

### Description of Sensitivity Map Files

We followed the file descriptions of (51) and generate HDF5 files with the same filenames as the original fastMRI dataset. We computed an extended set of coil sensitivity maps ( $M=2$ ) according to Uecker et al. (4). The sensitivity maps were computed on the ACLs, defined by `num_low_frequency`. For training and validation data `num_low_frequency` was set to 30, used for acceleration factor  $R=4$ , and 15, for  $R=8$ , respectively. For testing and challenge data, the `num_low_frequency` was defined in the HDF5 raw data files. Following data are stored in a single HDF5 files:

**reference\_acl{num\_low\_frequency}** [ $N_{\text{sl}}$ ,  $M$ ,  $N_{\text{FE}}$ ,  $N_{\text{PE}}$ ]. Coil-combined reference reconstruction. This dataset is only available for training and validation.

**smaps\_acl{num\_low\_frequency}** [ $N_{\text{sl}}$ ,  $Q$ ,  $M$ ,  $N_{\text{FE}}$ ,  $N_{\text{PE}}$ ]. Estimated coil sensitivity maps.

**ismrmrd\_header** XML header copied from the original HDF5 raw data file.

**norm\_lfimg\_max\_acl{num\_low\_frequency}** Attribute. Maximum intensity of the [ $N_{\text{sl}}$ , 320, 320] coil-combined low frequency reconstruction.

**norm\_lfimg\_mean\_acl{num\_low\_frequency}** Attribute. Mean complex intensity of the [ $N_{\text{sl}}$ , 320, 320] coil-combined low frequency reconstruction for the first sensitivity map.

**norm\_lfimg\_cov\_acl{num\_low\_frequency}** Attribute. Complex pseudo-covariance of the [ $N_{\text{sl}}$ , 320, 320] coil-combined low frequency reconstruction for the first sensitivity map.

**reference\_max\_acl{num\_low\_frequency}** Maximum magnitude value of the [ $N_{\text{sl}}$ , 320, 320] coil-combined fully sampled reconstruction. This attribute is only available for training and validation.

**rss\_max** Maximum value of the [ $N_{\text{sl}}$ , 320, 320] RSS reconstruction. This attribute is only available for training and validation.

## REFERENCES

1. Sodickson DK, Manning WJ. Simultaneous Acquisition of Spatial Harmonics (SMASH): Fast Imaging With Radiofrequency Coil Arrays. *Magnetic Resonance in Medicine* 1997;38(4):591–603.
2. Pruessmann KP, Weiger M, Boernert P, Boesiger P. Advances in Sensitivity Encoding With Arbitrary k-Space Trajectories. *Magnetic Resonance in Medicine* 2001;46(4):638–651.
3. Griswold MA, Jakob PM, Heidemann RM, Nittka M, Jellus V, Wang J, Kiefer B, Haase A. Generalized Autocalibrating Partially Parallel Acquisitions (GRAPPA). *Magnetic Resonance in Medicine* 2002;47(6):1202–1210.
4. Uecker M, Lai P, Murphy MJ, Virtue P, Elad M, Pauly JM, Vasanawala SS, Lustig M. ESPIRiT—An Eigenvalue Approach to Autocalibrating Parallel MRI: Where SENSE Meets GRAPPA. *Magnetic Resonance in Medicine* 2014; 71(3):990–1001.
5. Lustig M, Santos JM, Donoho DL, Pauly JM. k-t SPARSE: High frame rate dynamic MRI exploiting spatio-temporal sparsity. In Proceedings of the International Society of Magnetic Resonance in Medicine. 2006; 2420.
6. Liang D, Liu B, Wang J, Ying L. Accelerating SENSE Using Compressed Sensing. *Magnetic Resonance in Medicine* 2009;62(6):1574–1584.
7. Murphy M, Alley M, Demmel J, Keutzer K, Vasanawala S, Lustig M. Fast  $\ell_1$ -SPIRiT Compressed Sensing Parallel Imaging MRI: Scalable Parallel Implementation and Clinically Feasible Runtime. *IEEE Transactions on Medical Imaging* 2012;31(6):1250–1262.
8. Shin PJ, Larson PEZ, Ohliger MA, Elad M, Pauly JM, Vigneron DB, Lustig M. Calibrationless Parallel Imaging Reconstruction Based on Structured Low-Rank Matrix Completion. *Magnetic Resonance in Medicine* 2014;72(4):959–970.
9. Haldar JP. Low-rank modeling of local  $k$ -space neighborhoods (loraks) for constrained mri. *IEEE Transactions on Medical Imaging* 2013;33(3):668–681.
10. Haldar JP, Zhuo J. P-LORAKS: Low-Rank Modeling of Local k-Space Neighborhoods With Rarallel Imaging Data. *Magnetic Resonance in Medicine* 2016; 75(4):1499–1514.
11. Jin KH, Lee D, Ye JC. A General Framework for Compressed Sensing and Parallel MRI Using Annihilating Filter Based Low-Rank Hankel Matrix. *IEEE Transactions on Computational Imaging* 2016;2(4):480–495.
12. Block KT, Uecker M, Frahm J. Undersampled Radial MRI with Multiple Coils. Iterative Image Reconstruction using a Total Variation Constraint. *Magnetic Resonance in Medicine* 2007;57(6):1086–1098.

13. Knoll F, Clason C, Bredies K, Uecker M, Stollberger R. Parallel Imaging with Nonlinear Reconstruction using Variational Penalties. *Magnetic Resonance in Medicine* 2012;67(1):34–41.
14. Ravishankar S, Bresler Y. Learning Sparsifying Transforms for Image Processing. *IEEE International Conference on Image Processing* 2012;61(5):681–684.
15. Caballero J, Price AN, Rueckert D, Hajnal JV. Dictionary Learning and Time Sparsity for Dynamic MR Data Reconstruction. *IEEE Transactions on Medical Imaging* 2014;33(4):979–994.
16. Hammernik K, Klatzer T, Kobler E, Recht MP, Sodickson DK, Pock T, Knoll F. Learning a Variational Network for Reconstruction of Accelerated MRI Data. *Magnetic Resonance in Medicine* 2018;79(6):3055–3071.
17. Wang S, Su Z, Ying L, Peng X, Zhu S, Liang F, Feng D, Liang D. Accelerating Magnetic Resonance Imaging Via Deep Learning. In *IEEE International Symposium on Biomedical Imaging (ISBI)*. 2016; 514–517.
18. Han Y, Yoo J, Kim HH, Shin HJ, Sung K, Ye JC. Deep learning with domain adaptation for accelerated projection-reconstruction MR. *Magnetic Resonance in Medicine* 2018;80(3):1189–1205.
19. Zhu B, Liu JZ, Cauley SF, Rosen BR, Rosen MS. Image reconstruction by domain-transform manifold learning. *Nature* 2018;555(7697):487–492.
20. Schlemper J, Yang G, Ferreira P, Scott A, McGill LA, Khalique Z, Gorodezky M, Roehl M, Keegan J, Pennell D, Firmin D, Rueckert D. Stochastic Deep Compressive Sensing for the Reconstruction of Diffusion Tensor Cardiac MRI. *arXiv preprint arXiv:180512064* 2018;.
21. Yang Y, Sun J, Li H, Xu Z. ADMM-Net: A Deep Learning Approach for Compressive Sensing MRI. In *Advances in Neural Information Processing Systems*. 2017; 10–18.
22. Zhao H, Gallo O, Frosio I, Kautz J. Loss Functions for Image Restoration with Neural Networks. *IEEE Transactions on Computational Imaging* 2016;3(1):47 – 57.
23. Hammernik K, Knoll F, Sodickson D, Pock T. L2 or Not L2: Impact of Loss Function Design for Deep Learning MRI Reconstruction. In *Proceedings of the International Society of Magnetic Resonance in Medicine*. 2017; 687.
24. Yang G, Yu S, Dong H, Slabaugh G, Dragotti PL, Ye X, Liu F, Arridge S, Keegan J, Guo Y, Firmin D. DAGAN: Deep De-Aliasing Generative Adversarial Networks for Fast Compressed Sensing MRI Reconstruction. *IEEE Transactions on Medical Imaging* 2018;37(6):1310–1321.
25. Liu F, Samsonov A. Data-Cycle-Consistent Adversarial Networks for High-

- Quality Reconstruction of Undersampled MRI Data. In ISMRM Workshop on Machine Learning. 2017; .
- 26. Quan TM, Nguyen-Duc T, Jeong WK. Compressed Sensing MRI Reconstruction using a Generative Adversarial Network with a Cyclic Loss. *IEEE Transactions on Medical Imaging* 2018;37(6):1488–1497.
  - 27. Seitzer M, Yang G, Schlemper J, Oktay O, Würfl T, Christlein V, Wong T, Mohiaddin R, Firmin D, Keegan J, Rueckert D, Maier A. Adversarial and perceptual refinement for compressed sensing MRI reconstruction. In Lecture Notes in Computer Science (including subseries Lecture Notes in Artificial Intelligence and Lecture Notes in Bioinformatics), volume 11070 LNCS. 2018; 232–240.
  - 28. Mardani M, Gong E, Cheng JY, Vasanawala SS, Zaharchuk G, Xing L, Pauly JM. Deep Generative Adversarial Neural Networks for Compressive Sensing (GANCS) MRI. *IEEE Transactions on Medical Imaging* 2019;38(1):167–179.
  - 29. Aggarwal HK, Mani MP, Jacob M. MoDL: Model Based Deep Learning Architecture for Inverse Problems. *IEEE Transactions on Medical Imaging* 2019; 38(2):394–405.
  - 30. Cheng JY, Mardani M, Alley MT, Pauly JM, Vasanawala SS. DeepSPIRiT: Generalized Parallel Imaging Using Deep Convolutional Neural Networks. In Proceedings of the International Society of Magnetic Resonance in Medicine. 2018; 570.
  - 31. Kwon K, Kim D, Park H. A parallel MR imaging method using multilayer perceptron:. *Medical Physics* 2017;44(12):6209–6224.
  - 32. Han Y, Ye JC. k-Space Deep Learning for Accelerated MRI. arXiv preprint arXiv:180503779 2018;1–11.
  - 33. Eo T, Jun Y, Kim T, Jang J, Lee HJ, Hwang D. KIKI-net: Cross-domain convolutional neural networks for reconstructing undersampled magnetic resonance images. *Magnetic Resonance in Medicine* 2018;80(5):2188–2201.
  - 34. Souza R, Lebel RM, Frayne R, Ca R. A Hybrid, Dual Domain, Cascade of Convolutional Neural Networks for Magnetic Resonance Image Reconstruction. *Proceedings of Machine Learning Research* 2019;102:437–446.
  - 35. Akçakaya M, Moeller S, Weingärtner S, Uğurbil K. Scan-specific robust artificial-neural-networks for k-space interpolation (RAKI) reconstruction: Database-free deep learning for fast imaging. *Magnetic Resonance in Medicine* 2019;81(1):439–453.
  - 36. Virtue P, Stella XY, Lustig M. Better than Real: Complex-valued Neural Nets for MRI Fingerprinting. In IEEE International Conference on Image Processing. IEEE, 2017; 3953–3957.

37. Wang S, Cheng H, Ying L, Xiao T, Ke Z, Liu X, Zheng H, Liang D. DeepcomplexMRI: Exploiting deep residual network for fast parallel MR imaging with complex convolution. arXiv preprint arXiv:190604359 2019;;
38. Sun L, Fan Z, Fu X, Huang Y, Ding X, Paisley J. A Deep Information Sharing Network for Multi-Contrast Compressed Sensing MRI Reconstruction. IEEE Transactions on Image Processing 2019;28(12):6141–6153.
39. Polak D, Cauley S, Bilgic B, Gong E, Bachert P, Adalsteinsson E, Setsompop K. Joint multi-contrast Variational Network reconstruction (jVN) with application to rapid 2D and 3D imaging. arXiv preprint arXiv:191003273 2019;;
40. Qin C, Schlemper J, Caballero J, Price AN, Hajnal JV, Rueckert D. Convolutional Recurrent Neural Networks for Dynamic MR Image Reconstruction. IEEE Transactions on Medical Imaging 2019;38(1):280–290.
41. Schlemper J, Caballero J, Hajnal JV, Price AN, Rueckert D. A Deep Cascade of Convolutional Neural Networks for Dynamic MR Image Reconstruction. IEEE Transactions on Medical Imaging 2018;37(2):491–503.
42. Qin C, Schlemper J, Duan J, Seegoolam G, Price A, Hajnal J, Rueckert D. k-t NEXT: Dynamic MR Image Reconstruction Exploiting Spatio-Temporal Correlations. In International Conference on Medical Image Computing and Computer-Assisted Intervention. Springer, 2019; 505–513.
43. Hauptmann A, Arridge S, Lucka F, Muthurangu V, Steeden JA. Real-time Cardiovascular MR with Spatio-temporal Artifact Suppression Using Deep Learning—Proof of Concept in Congenital Heart Disease. Magnetic Resonance in Medicine 2019;81(2):1143–1156.
44. Jin KH, Gupta H, Yerly J, Stuber M, Unser M. Time-Dependent Deep Image Prior for Dynamic MRI. arXiv preprint arXiv:191001684 2019;;
45. Kofler A, Dewey M, Schaeffter T, Wald C, Kolbitsch C. Spatio-Temporal Deep Learning-Based Undersampling Artefact Reduction for 2D Radial Cine MRI with Limited Data. arXiv preprint arXiv:190401574 2019;;
46. Cohen O, Zhu B, Rosen MS. MR fingerprinting Deep RecOnstruction NEtwork (DRONE). Magnetic Resonance in Medicine 2018;80(3):885–894.
47. Knoll F, Hammernik K, Zhang C, Moeller S, Pock T, Sodickson DK, Akcakaya M. Deep Learning Methods for Parallel Magnetic Resonance Image Reconstruction. arXiv preprint arXiv:190401112 2019;;
48. Hammernik K, Knoll F. Machine Learning for Image Reconstruction. In D Rueckert, G Fichtinger, SK Zhou, eds., Handbook of Medical Image Computing and Computer Assisted Intervention. Elsevier, 2018; 25–64.
49. Liang D, Cheng J, Ke Z, Ying L. Deep MRI Reconstruction: Unrolled Opti-

- mization Algorithms Meet Neural Networks. arXiv preprint arXiv:190711711 2019;.
- 50. Lundervold AS, Lundervold A. An overview of deep learning in medical imaging focusing on MRI. *Zeitschrift für Medizinische Physik* 2019;29(2):102–127.
  - 51. Zbontar J, Knoll F, Sriram A, Muckley MJ, Bruno M, Defazio A, Parente M, Geras KJ, Katsnelson J, Chandarana H, Zhang Z, Drozdal M, Romero A, Rabbat M, Vincent P, Pinkerton J, Wang D, Yakubova N, Owens E, Zitnick CL, Recht MP, Sodickson DK, Lui YW. fastMRI: An Open Dataset and Benchmarks for Accelerated MRI. arXiv preprint arXiv:181108839 2018;.
  - 52. Putzky P, Welling M. Invert to Learn to Invert. In *Advances in Neural Information Processing Systems*. 2019; 444–454.
  - 53. Bahadir CD, Dalca AV, Sabuncu MR. Adaptive Compressed Sensing MRI with Unsupervised Learning. arXiv preprint arXiv:190711374 2019;.
  - 54. Sriram A, Zbontar J, Murrell T, Zitnick CL, Defazio A, Sodickson DK. GraphpaNet: Combining Parallel Imaging with Deep Learning for Multi-Coil MRI Reconstruction. arXiv preprint arXiv:191012325 2019;.
  - 55. Wang P, Chen EZ, Chen T, Patel VM, Sun S. Pyramid Convolutional RNN for MRI Reconstruction. arXiv preprint arXiv:191200543 2019;.
  - 56. Roemer PB, Edelstein WA, Hayes CE, Souza SP, Mueller OM. The NMR Phased Array. *Magnetic Resonance in Medicine* 1990;16(2):192–225.
  - 57. Robson PM, Grant AK, Madhuranthakam AJ, Lattanzi R, Sodickson DK, McKenzie CA. Comprehensive Quantification of Signal-to-Noise Ratio and g-Factor for Image-based and k-Space-based Parallel Imaging Reconstructions. *Magnetic Resonance in Medicine* 2008;60(4):895–907.
  - 58. Jin KH, McCann MT, Froustey E, Unser M. Deep Convolutional Neural Network for Inverse Problems in Imaging. *IEEE Transactions on Image Processing* 2017;26(9):4509–4522.
  - 59. Lee D, Yoo J, Ye JC. Deep residual learning for compressed sensing MRI. In *IEEE International Symposium on Biomedical Imaging*. 2017; 15–18.
  - 60. Schlemper J, Duan J, Ouyang C, Qin C, Caballero J, Hajnal JV, Rueckert D. Data Consistency Networks for (Calibration-less) Accelerated Parallel MR Image Reconstruction. In *Proceedings of the International Society of Magnetic Resonance in Medicine*. 2019; 4664.
  - 61. Duan J, Schlemper J, Qin C, Ouyang C, Bai W, Biffi C, Bello G, Statton B, O'Regan DP, Rueckert D. VS-Net: Variable Splitting Network for Accelerated Parallel MRI Reconstruction. In *International Conference on Medical Image Computing and Computer-Assisted Intervention*. 2019; 713–722.

62. Schlemper J, Qin C, Duan J, Summers RM, Hammernik K.  $\Sigma$ -net: Ensembled Iterative Deep Neural Networks for Accelerated Parallel MR Image Reconstruction. arXiv preprint arXiv:191205480 2019;.
63. Ronneberger O, Fischer P, Brox T. U-Net: Convolutional Networks for Biomedical Image Segmentation. In International Conference on Medical Image Computing and Computer Assisted Intervention. 2015; 234–241.
64. Yu S, Park B, Jeong J. Deep Iterative Down-Up CNN for Image Denoising. In Proceedings of the IEEE Conference on Computer Vision and Pattern Recognition Workshops. 2019; .
65. Abdelhamed A, Timofte R, Brown MS. NTIRE 2019 Challenge on Real Image Denoising: Methods and Results. In Proceedings of the IEEE Conference on Computer Vision and Pattern Recognition Workshops. 2019; .
66. Shi W, Caballero J, Huszar F, Totz J, Aitken AP, Bishop R, Rueckert D, Wang Z. Real-Time Single Image and Video Super-Resolution Using an Efficient Sub-Pixel Convolutional Neural Network. In Proceedings of the IEEE Computer Society Conference on Computer Vision and Pattern Recognition, volume 2016-Decem. 2016; 1874–1883.
67. Zhang Y, Li K, Li K, Wang L, Zhong B, Fu Y. Image Super-Resolution Using Very Deep Residual Channel Attention Networks. In Lecture Notes in Computer Science (including subseries Lecture Notes in Artificial Intelligence and Lecture Notes in Bioinformatics), volume 11211 LNCS. 2018; 294–310.
68. Haris M, Shakhnarovich G, Ukita N. Deep Back-Projection Networks for Super-Resolution. In Proceedings of the IEEE Conference on Computer Vision and Pattern Recognition. 2018; 1664–1673.
69. Shi W, Caballero J, Theis L, Huszar F, Aitken A, Ledig C, Wang Z. Is the deconvolution layer the same as a convolutional layer? arXiv preprint arXiv:160907009 2016;.
70. Trabelsi C, Bilaniuk O, Zhang Y, Serdyuk D, Subramanian S, Santos JF, Mehri S, Rostamzadeh N, Bengio Y, Pal CJ. Deep Complex Networks. arXiv preprint arXiv:170509792 2017;.
71. Wang X, Yu K, Wu S, Gu J, Liu Y, Dong C, Qiao Y, Change Loy C. ESRGAN: Enhanced Super-Resolution Generative Adversarial Networks. In Proceedings of the European Conference on Computer Vision Workshops. 2018; .
72. Huang G, Liu Z, Van Der Maaten L, Weinberger KQ. Densely Connected Convolutional Networks. In Proceedings of the IEEE Conference on Computer Vision and Pattern Recognition. 2017; 2261–2269.
73. Zhang Y, Tian Y, Kong Y, Zhong B, Fu Y. Residual Dense Network for Image

- Super-Resolution. In Proceedings of the IEEE Computer Society Conference on Computer Vision and Pattern Recognition. 2018; 2472–2481.
- 74. Mao X, Li Q, Xie H, Lau RYK, Wang Z, Smolley SP. Least Squares Generative Adversarial Networks. In Proceedings of the IEEE International Conference on Computer Vision. 2017; 2794–2802.
  - 75. Ledig C, Theis L, Huszár F, Caballero J, Cunningham A, Acosta A, Aitken A, Tejani A, Totz J, Wang Z, Shi Twitter W. Photo-Realistic Single Image Super-Resolution Using a Generative Adversarial Network. In IEEE Conference on Computer Vision and Pattern Recognition. 2017; 4681–4690.
  - 76. Ulyanov D, Vedaldi A, Lempitsky V. Deep Image Prior. In Proceedings of the IEEE Conference on Computer Vision and Pattern Recognition. 2018; 9446–9454.
  - 77. Mataev G, Elad M, Milanfar P. DeepRED: Deep Image Prior Powered by RED. arXiv preprint arXiv:190310176 2019;.
  - 78. Goodfellow I, Bengio Y, Courville A. Deep Learning. MIT Press, 2016.
  - 79. Krizhevsky A, Sutskever I, Geoffrey E H. ImageNet Classification with Deep Convolutional Neural Networks. In Advances in Neural Information Processing Systems. 2012; 1097–1105.
  - 80. Rother C, Kolmogorov V, Blake A. GrabCut - Interactive Foreground Extraction Using Iterated Graph Cuts. In ACM SIGGRAPH, volume 23. 2004; 309–314.
  - 81. Friedman M. The Use of Ranks to Avoid the Assumption of Normality Implicit in the Analysis of Variance. Journal of the American Statistical Association 1937;32(200):675–701.
  - 82. Wilcoxon F. Individual Comparisons by Ranking Methods. In Biometrics Bulletin, volume 1. Springer, 1945; 80.
  - 83. Stikov N, Trzasko JD, Bernstein MA. Reproducibility and the future of MRI research. Magnetic Resonance in Medicine 2019;82(6):1981–1983.
  - 84. Uecker M, Ong F, Tamir JI, Bahri D, Virtue P, Cheng JY, Zhang T, Lustig M. Berkeley Advanced Reconstruction Toolbox. In Proceedings of the International Society of Magnetic Resonance in Medicine. 2015; 2486.
  - 85. Shitrit O, Riklin Raviv T. Accelerated magnetic resonance imaging by adversarial neural network. In Lecture Notes in Computer Science (including subseries Lecture Notes in Artificial Intelligence and Lecture Notes in Bioinformatics), volume 10553 LNCS. Springer, Cham, 2017; 30–38.
  - 86. Hammernik K, Kobler E, Pock T, Recht M, Sodickson DK, Knoll F. Variational Adversarial Networks for Accelerated MR Image Reconstruction. In Proceedings of the International Society of Magnetic Resonance in Medicine. 2018; 1091.

87. Caballero J, Bai W, Price AN, Rueckert D, Hajnal JV. Application-driven MRI: Joint Reconstruction and Segmentation From Undersampled MRI Data. In International Conference on Medical Image Computing and Computer-Assisted Intervention. Springer, 2014; 106–113.
88. Schlemper J, Oktay O, Bai W, Castro DC, Duan J, Qin C, Hajnal JV, Rueckert D. Cardiac MR Segmentation From Undersampled k-Space Using Deep Latent Representation Learning. In International Conference on Medical Image Computing and Computer-Assisted Intervention. Springer, 2018; 259–267.
89. Antun V, Renna F, Poon C, Adcock B, Hansen AC. On instabilities of deep learning in image reconstruction—Does AI come at a cost? arXiv preprint arXiv:190205300 2019;.

## LIST OF FIGURES

- Figure 1. Structure of the Down-Up Network (DUN) block for MR image reconstruction with arbitrary DC layers. This block is repeated in an iterative manner. Parameters over the single iterations can be shared or variable. Characteristic element is the concatenated Down-Up Block (DUB), consisting of numerous residual blocks at various scales.
- Figure 2. Structure of Sensitivity Networks (SNs) and Parallel Coil Networks (PCNs). While the combination of individual coil elements is done in the DC layer in SNs using explicit coil sensitivity maps, the NN realizes the coil combination in PCNs.
- Figure 3. Comparison of different DC terms for a coronal PDFS case and acceleration  $R=4$  (`multicoil_val/file1000990.h5`, slice 19). We observe a substantial difference between image enhancement and image reconstruction networks in terms of blurring and depicted anatomy. The lateral meniscus, indicated by the green arrow, shows a gap for image enhancement networks compared to reconstruction networks. We observe no substantial differences between different DC layers.  $SN_{PG}^{8s}$  contains more noise and appears slightly sharper than the other reconstructions.
- Figure 4. Comparison of different DC terms for a coronal PD case and acceleration  $R=8$  (`multicoil_val/file1002351.h5`, slice 23). We observe a substantial difference between image enhancement and image reconstruction networks in terms of blurring and depicted anatomy. The area in the lateral aspect of the knee, indicated by the green arrows, shows a substantial deviation of anatomy for image enhancement networks, more prominent for  $SN_{ID}^8$ . We observe no substantial differences between different DC layers.  $SN_{PG}^{8s}$  appears slightly sharper than the other reconstructions.
- Figure 5. Detailed view of the depicted cases in Figure 3 and Figure 4 for image enhancement and image reconstruction. We clearly observe the deviations in anatomy for the image enhancement network in both contrasts and acceleration factors. The area in the lateral meniscus, indicated by the green arrow, is depicted neither in the image enhancement  $SN_{ID}^8$  nor the reconstruction network  $SN_{GD}^8$  for this high acceleration factor of  $R=8$ .

Figure 6. We show the influence of different learning schemes on a PDFS case (`multicoil_val/file1000114.h5` for acceleration factor  $R=8$  on the full knee, along with zoomed regions of the lateral and medial meniscus and the intercondylar notch. We observe that the image for  $\text{SN}_{\text{GD}}^8$  is most blurred, and texture is increased for both  $\text{SN}_{\text{GD-FT}}^8$  and  $\text{SN}_{\text{GD-GAN}}^8$ . The  $\text{SN}_{\text{GD-GAN}}^8$  result appears most textured. The  $\Sigma\text{-net}^8$  results exploit the advantages of all included network architectures and show also improved texture compared to the  $\text{SN}_{\text{GD}}^8$  network, while maintaining the quantitative scores as depicted in Table 2.

## LIST OF TABLES

- Table 1. Comparison of SNs and PCNs for different DC layers, number of cascades as well as shared and variable parameters. Reconstruction networks with any DC, i.e., GD, PG or VS, clearly outperform image enhancement networks.
- Table 2. Influence of supervised learning with standard loss, adversarial loss and semi-supervised fine-tuning. By adding an adversarial loss, denoted by GAN, or using fine-tuning, the quantitative values drop for all cases.

## LIST OF SUPPORTING FIGURES

- S. Figure S1. Examples of the heterogeneous fastMRI (51) training and validation set for coronal knee scans. The data have different number of PE lines according to the acquisition.
- S. Figure S2. Comparison of fully-sampled RSS reconstruction (left), which is the reference of the fastMRI challenge, and the fully-sampled sensitivity-combined reconstruction (SENSE) (right). The SSIM between the two fully sampled scan is 0.6979, respectively. Although only foreground information is important, the background is also included in evaluation and has, however, a huge influence on the quantitative scores. Removing the background in both RSS and SENSE already yields an substantial increase of the SSIM to 0.9625.

S. Figure S3. `multicoil_val/file1000206.h5` slice 24  $R=4$ : This figure depicts reconstruction results for different network architectures along with the dataterm argument  $Ax - y$  of a selected coil. We observe huge deviations in  $k$ -space for  $\text{SN}_{\text{ID}}^8$ . The  $k$ -space for  $\text{SN}_{\text{GD}}^8$  and  $\text{SN}_{\text{GD-FT}}^8$  appear similar. The  $\mathcal{D}$ -NMSE is lowest for  $\text{SN}_{\text{GD-FT}}^8$ , indicating that the reconstruction adapted to the new  $k$ -space data. Although the  $\mathcal{D}$ -NMSE is lower for  $\text{SN}_{\text{GD-GAN}}^8$  than for  $\text{SN}_{\text{GD}}^8$  we observe a subtle, bright spot in the center of  $k$ -space of  $\text{SN}_{\text{GD-GAN}}^8$ , which might indicate a deviation from the ground truth for this particular slice. Note that despite better texture, the drop in SSIM of  $\text{SN}_{\text{GD-FT}}^8$  from  $\text{SN}_{\text{GD}}^8$  is expected, and is consistent with Equation [6].

## LIST OF SUPPORTING TABLES

S. Table S1. Comparison of the number of parameters for U-net and DUN. The number of parameters for one cascades equals the number of parameters for arbitrary cascades and shared parameters. The U-net and DUN have approximately the same model capacity. The model capacity for SNs and PCNs are also comparable.

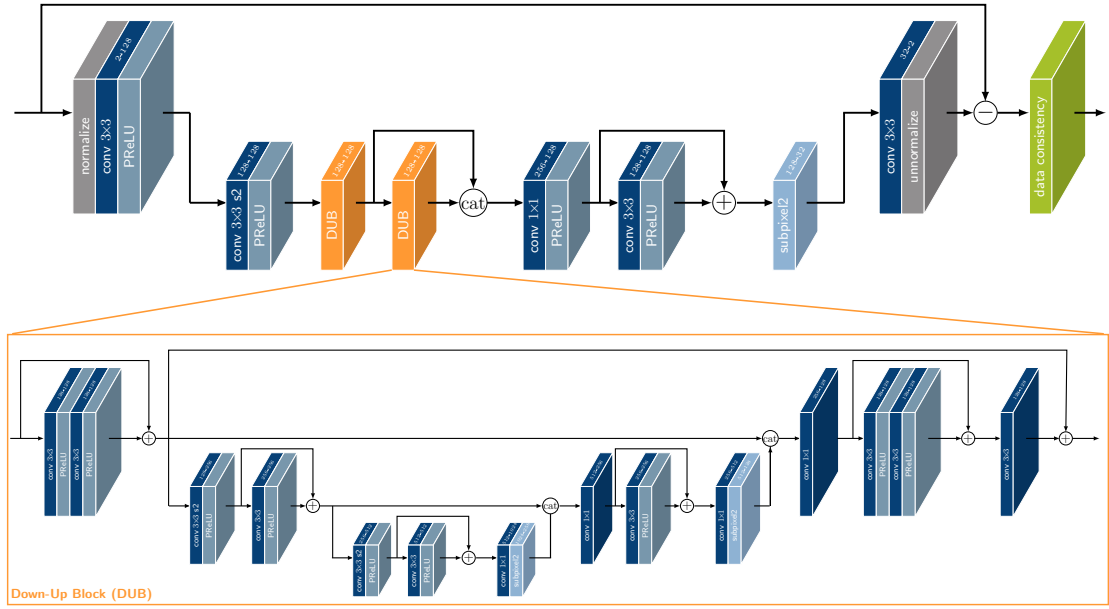


Figure 1: Structure of the Down-Up Network (DUN) block for MR image reconstruction with arbitrary DC layers. This block is repeated in an iterative manner. Parameters over the single iterations can be shared or variable. Characteristic element is the concatenated Down-Up Block (DUB), consisting of numerous residual blocks at various scales.

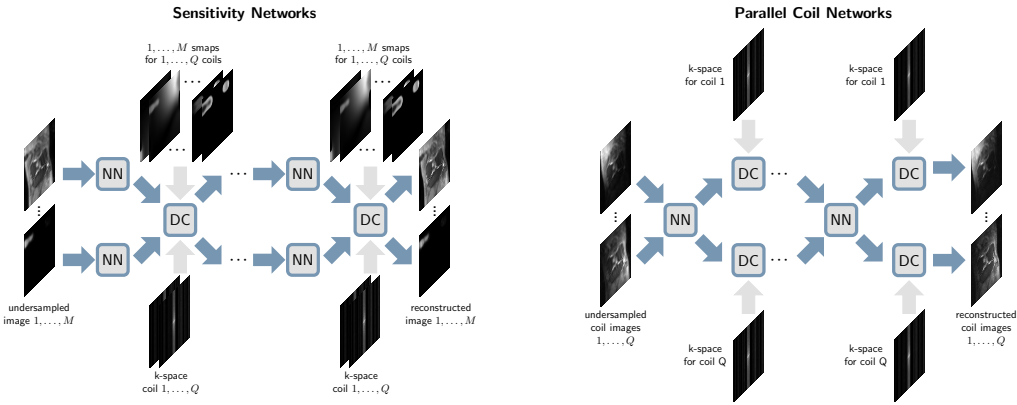


Figure 2: Structure of Sensitivity Networks (SNs) and Parallel Coil Networks (PCNs). While the combination of individual coil elements is done in the DC layer in SNs using explicit coil sensitivity maps, the NN realizes the coil combination in PCNs.

Table 1: Comparison of SNs and PCNs for different DC layers, number of cascades as well as shared and variable parameters. Reconstruction networks with any DC, i.e., GD, PG or VS, clearly outperform image enhancement networks.

Model	Contrast	R=4			R=8		
		NMSE	PSNR	SSIM	NMSE	PSNR	SSIM
UNET	ALL	0.0152 ± 0.0094	34.95 ± 1.94	0.9094 ± 0.0281	0.0288 ± 0.0137	31.94 ± 1.78	0.8621 ± 0.0342
	PD	0.0104 ± 0.0034	34.85 ± 2.07	0.9251 ± 0.0191	0.0220 ± 0.0061	31.53 ± 1.81	0.8780 ± 0.0271
	PDFS	0.0200 ± 0.0110	35.05 ± 1.79	0.8936 ± 0.0270	0.0358 ± 0.0157	32.36 ± 1.66	0.8461 ± 0.0332
$SN_{ID}^s$	ALL	0.0152 ± 0.0097	34.98 ± 1.92	0.9099 ± 0.0281	0.0277 ± 0.0129	32.12 ± 1.75	0.8633 ± 0.0342
	PD	0.0101 ± 0.0035	34.99 ± 2.06	0.9257 ± 0.0192	0.0210 ± 0.0066	31.75 ± 1.77	0.8791 ± 0.0268
	PDFS	0.0204 ± 0.0112	34.98 ± 1.77	0.8939 ± 0.0267	0.0345 ± 0.0142	32.50 ± 1.65	0.8473 ± 0.0335
$SN_{ID}^{ss}$	ALL	0.0144 ± 0.0070	35.15 ± 2.00	0.9153 ± 0.0277	0.0255 ± 0.0106	32.49 ± 1.86	0.8718 ± 0.0344
	PD	0.0111 ± 0.0059	34.84 ± 2.05	0.9315 ± 0.0172	0.0200 ± 0.0089	32.09 ± 1.84	0.8898 ± 0.0248
	PDFS	0.0177 ± 0.0064	35.46 ± 1.91	0.8989 ± 0.0268	0.0311 ± 0.0093	32.89 ± 1.81	0.8536 ± 0.0333
$SN_{GD}^{ss}$	ALL	0.0069 ± 0.0046	38.90 ± 2.41	0.9351 ± 0.0308	0.0148 ± 0.0075	35.10 ± 1.92	0.8920 ± 0.0369
	PD	0.0033 ± 0.0015	40.01 ± 2.16	0.9564 ± 0.0153	0.0092 ± 0.0037	35.45 ± 1.87	0.9145 ± 0.0233
	PDFS	0.0104 ± 0.0037	37.77 ± 2.13	0.9136 ± 0.0273	0.0204 ± 0.0062	34.74 ± 1.92	0.8692 ± 0.0341
$SN_{PG}^{ss}$	ALL	0.0067 ± 0.0048	39.17 ± 2.62	0.9362 ± 0.0327	0.0131 ± 0.0075	35.78 ± 2.08	0.8987 ± 0.0391
	PD	0.0029 ± 0.0014	40.54 ± 2.25	0.9594 ± 0.0156	0.0074 ± 0.0030	36.44 ± 1.94	0.9245 ± 0.0222
	PDFS	0.0105 ± 0.0039	37.78 ± 2.20	0.9128 ± 0.0285	0.0189 ± 0.0060	35.10 ± 2.01	0.8726 ± 0.0350
$SN_{VS}^{ss}$	ALL	0.0074 ± 0.0047	38.50 ± 2.28	0.9337 ± 0.0306	0.0148 ± 0.0076	35.10 ± 1.96	0.8939 ± 0.0372
	PD	0.0037 ± 0.0015	39.49 ± 2.08	0.9549 ± 0.0153	0.0091 ± 0.0035	35.51 ± 1.92	0.9173 ± 0.0230
	PDFS	0.0111 ± 0.0038	37.49 ± 2.03	0.9124 ± 0.0272	0.0206 ± 0.0061	34.69 ± 1.92	0.8703 ± 0.0338
$PCN_{PG}^{ss}$	ALL	0.0077 ± 0.0052	38.38 ± 2.34	0.9288 ± 0.0333	0.0148 ± 0.0077	35.12 ± 1.90	0.8905 ± 0.0379
	PD	0.0037 ± 0.0016	39.49 ± 2.05	0.9518 ± 0.0162	0.0089 ± 0.0032	35.55 ± 1.80	0.9143 ± 0.0226
	PDFS	0.0118 ± 0.0043	37.25 ± 2.07	0.9056 ± 0.0299	0.0207 ± 0.0062	34.68 ± 1.91	0.8665 ± 0.0350
$SN_{ID}^s$	ALL	0.0102 ± 0.0049	36.67 ± 1.81	0.9182 ± 0.0281	0.0209 ± 0.0081	33.31 ± 1.71	0.8745 ± 0.0341
	PD	0.0066 ± 0.0022	36.88 ± 1.76	0.9350 ± 0.0169	0.0156 ± 0.0049	33.04 ± 1.68	0.8922 ± 0.0240
	PDFS	0.0139 ± 0.0041	36.46 ± 1.84	0.9012 ± 0.0269	0.0263 ± 0.0070	33.59 ± 1.71	0.8566 ± 0.0335
$SN_{GD}^s$	ALL	0.0063 ± 0.0044	39.37 ± 2.53	0.9391 ± 0.0307	0.0126 ± 0.0070	35.88 ± 2.00	0.9025 ± 0.0369
	PD	0.0029 ± 0.0013	40.65 ± 2.18	0.9608 ± 0.0142	0.0074 ± 0.0030	36.44 ± 1.91	0.9266 ± 0.0210
	PDFS	0.0098 ± 0.0036	38.08 ± 2.18	0.9172 ± 0.0270	0.0180 ± 0.0056	35.31 ± 1.94	0.8781 ± 0.0334
$SN_{PG}^s$	ALL	0.0071 ± 0.0045	38.62 ± 2.27	0.9353 ± 0.0303	0.0149 ± 0.0075	35.04 ± 1.89	0.8941 ± 0.0367
	PD	0.0036 ± 0.0015	39.55 ± 2.06	0.9561 ± 0.0150	0.0093 ± 0.0036	35.39 ± 1.86	0.9169 ± 0.0225
	PDFS	0.0107 ± 0.0038	37.67 ± 2.09	0.9142 ± 0.0270	0.0206 ± 0.0061	34.69 ± 1.86	0.8710 ± 0.0337
$SN_{VS}^s$	ALL	0.0070 ± 0.0046	38.74 ± 2.34	0.9363 ± 0.0303	0.0147 ± 0.0077	35.15 ± 1.89	0.8954 ± 0.0367
	PD	0.0034 ± 0.0015	39.81 ± 2.12	0.9574 ± 0.0147	0.0089 ± 0.0036	35.60 ± 1.87	0.9186 ± 0.0224
	PDFS	0.0107 ± 0.0037	37.66 ± 2.04	0.9150 ± 0.0268	0.0206 ± 0.0062	34.69 ± 1.82	0.8719 ± 0.0333
$PCN_{PG}^s$	ALL	0.0072 ± 0.0048	38.70 ± 2.41	0.9332 ± 0.0315	0.0142 ± 0.0074	35.31 ± 1.92	0.8940 ± 0.0370
	PD	0.0034 ± 0.0015	39.85 ± 2.11	0.9551 ± 0.0154	0.0086 ± 0.0032	35.74 ± 1.82	0.9172 ± 0.0221
	PDFS	0.0110 ± 0.0039	37.55 ± 2.13	0.9111 ± 0.0280	0.0198 ± 0.0060	34.86 ± 1.92	0.8705 ± 0.0341

Table 2: Influence of supervised learning with standard loss, adversarial loss and semi-supervised fine-tuning. By adding an adversarial loss, denoted by GAN, or using fine-tuning, the quantitative values drop for all cases.

Model	Contrast	R=4			R=8		
		NMSE	PSNR	SSIM	NMSE	PSNR	SSIM
$SN_{GD}^s$	ALL	0.0063 ± 0.0044	39.37 ± 2.53	0.9391 ± 0.0307	0.0126 ± 0.0070	35.88 ± 2.00	0.9025 ± 0.0369
	PD	0.0029 ± 0.0013	40.65 ± 2.18	0.9608 ± 0.0142	0.0074 ± 0.0030	36.44 ± 1.91	0.9266 ± 0.0210
	PDFS	0.0098 ± 0.0036	38.08 ± 2.18	0.9172 ± 0.0270	0.0180 ± 0.0056	35.31 ± 1.94	0.8781 ± 0.0334
$SN_{GD-GAN}^s$	ALL	0.0072 ± 0.0052	38.86 ± 2.60	0.9333 ± 0.0336	0.0151 ± 0.0084	35.14 ± 2.02	0.8883 ± 0.0406
	PD	0.0031 ± 0.0014	40.34 ± 2.15	0.9580 ± 0.0148	0.0084 ± 0.0033	35.85 ± 1.88	0.9158 ± 0.0232
	PDFS	0.0114 ± 0.0040	37.37 ± 2.14	0.9083 ± 0.0283	0.0219 ± 0.0063	34.42 ± 1.91	0.8606 ± 0.0352
$SN_{GD-FT}^s$	ALL	0.0070 ± 0.0049	38.87 ± 2.48	0.9338 ± 0.0323	0.0135 ± 0.0075	35.61 ± 2.01	0.8978 ± 0.0388
	PD	0.0032 ± 0.0014	40.10 ± 2.13	0.9567 ± 0.0151	0.0077 ± 0.0031	36.21 ± 1.89	0.9238 ± 0.0216
	PDFS	0.0109 ± 0.0040	37.63 ± 2.17	0.9107 ± 0.0284	0.0193 ± 0.0061	35.00 ± 1.95	0.8716 ± 0.0345
$\Sigma\text{-net}^s$	ALL	0.0065 ± 0.0045	39.28 ± 2.53	0.9386 ± 0.0309	0.0128 ± 0.0071	35.85 ± 2.02	0.9018 ± 0.0373
	PD	0.0029 ± 0.0013	40.56 ± 2.19	0.9605 ± 0.0143	0.0074 ± 0.0030	36.45 ± 1.93	0.9263 ± 0.0213
	PDFS	0.0100 ± 0.0037	37.98 ± 2.17	0.9165 ± 0.0271	0.0183 ± 0.0057	35.23 ± 1.93	0.8770 ± 0.0335

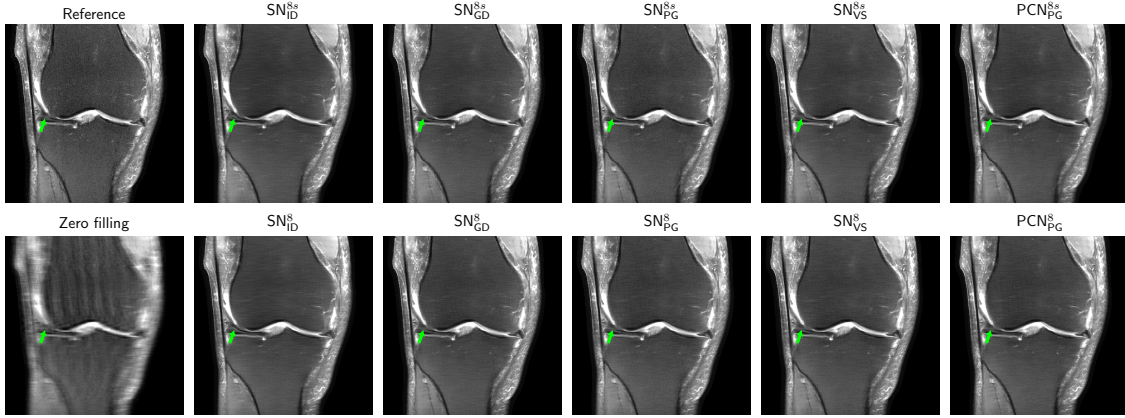


Figure 3: Comparison of different DC terms for a coronal PDFS case and acceleration  $R=4$  (`multicoil_val/file1000990.h5`, slice 19). We observe a substantial difference between image enhancement and image reconstruction networks in terms of blurring and depicted anatomy. The lateral meniscus, indicated by the green arrow, shows a gap for image enhancement networks compared to reconstruction networks. We observe no substantial differences between different DC layers.  $SN_{PG}^{8s}$  contains more noise and appears slightly sharper than the other reconstructions.

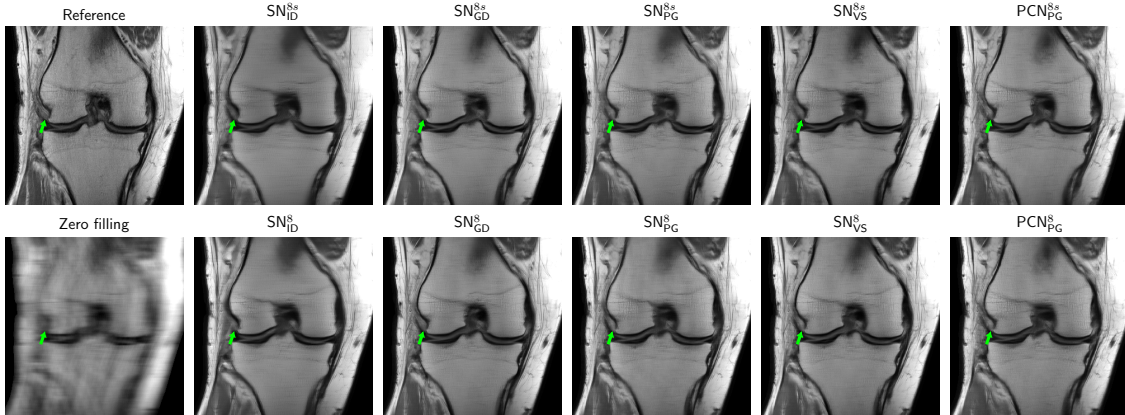


Figure 4: Comparison of different DC terms for a coronal PD case and acceleration  $R=8$  (`multicoil_val/file1002351.h5`, slice 23). We observe a substantial difference between image enhancement and image reconstruction networks in terms of blurring and depicted anatomy. The area in the lateral aspect of the knee, indicated by the green arrows, shows a substantial deviation of anatomy for image enhancement networks, more prominent for  $SN_{ID}^{8s}$ . We observe no substantial differences between different DC layers.  $SN_{PG}^{8s}$  appears slightly sharper than the other reconstructions.

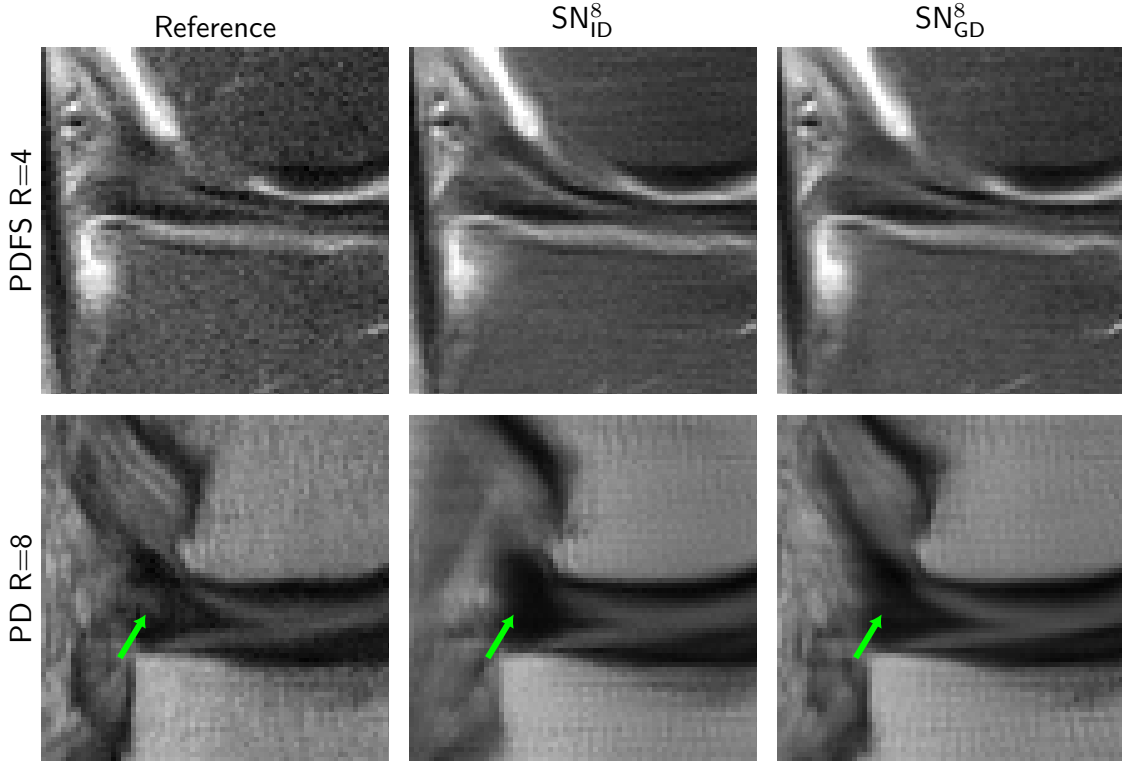


Figure 5: Detailed view of the depicted cases in Figure 3 and Figure 4 for image enhancement and image reconstruction. We clearly observe the deviations in anatomy for the image enhancement network in both contrasts and acceleration factors. The area in the lateral meniscus, indicated by the green arrow, is depicted neither in the image enhancement  $SN_{ID}^8$  nor the reconstruction network  $SN_{GD}^8$  for this high acceleration factor of  $R=8$ .

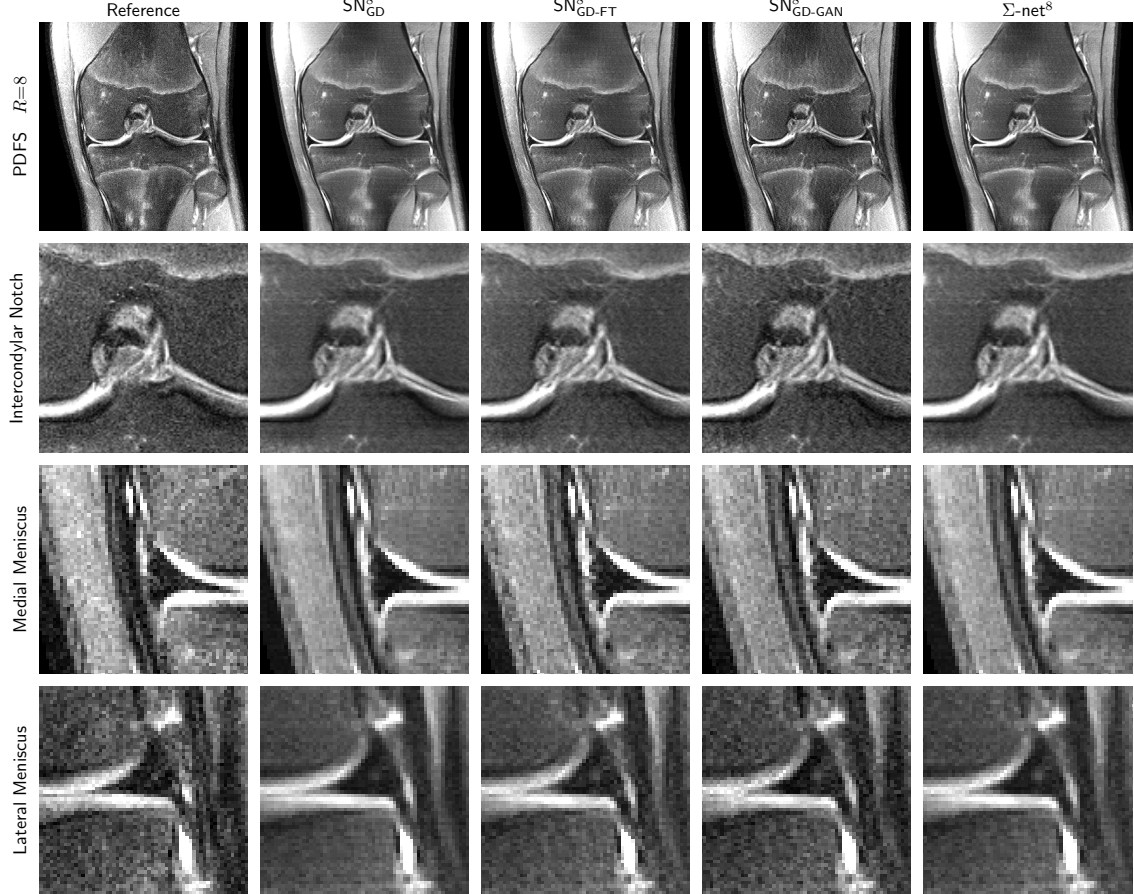
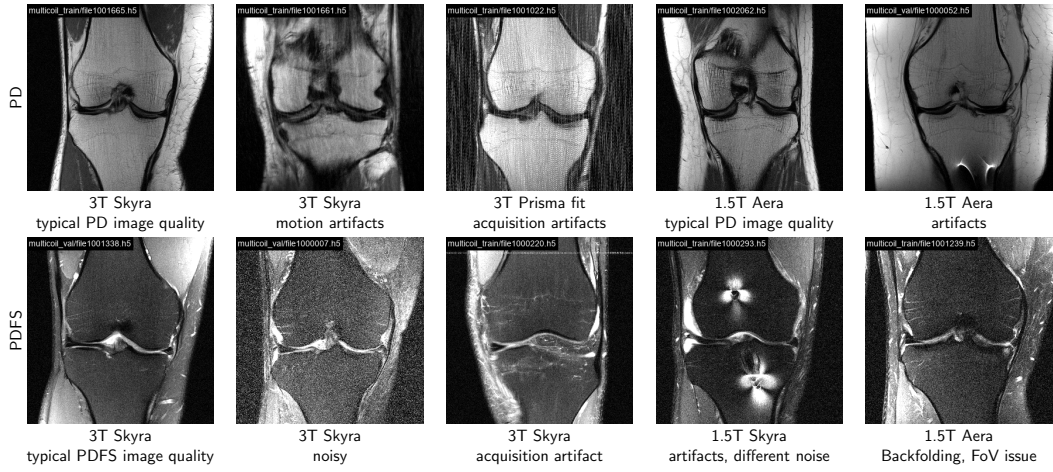
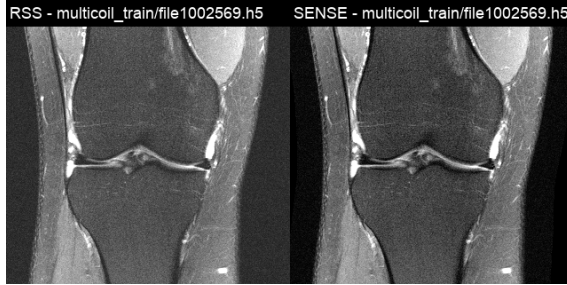


Figure 6: We show the influence of different learning schemes on a PDFS case (`multicoil_val/file1000114.h5` for acceleration factor  $R=8$  on the full knee, along with zoomed regions of the lateral and medial meniscus and the intercondylar notch. We observe that the image for  $SN_{GD}^8$  is most blurred, and texture is increased for both  $SN_{GD-FT}^8$  and  $SN_{GD-GAN}^8$ . The  $SN_{GD-GAN}^8$  result appears most textured. The  $\Sigma$ -net $^8$  results exploit the advantages of all included network architectures and show also improved texture compared to the  $SN_{GD}^8$  network, while maintaining the quantitative scores as depicted in Table 2.

$\Sigma$ -net: Systematic Evaluation of Iterative Deep Neural Networks for Fast Parallel MR Image Reconstruction



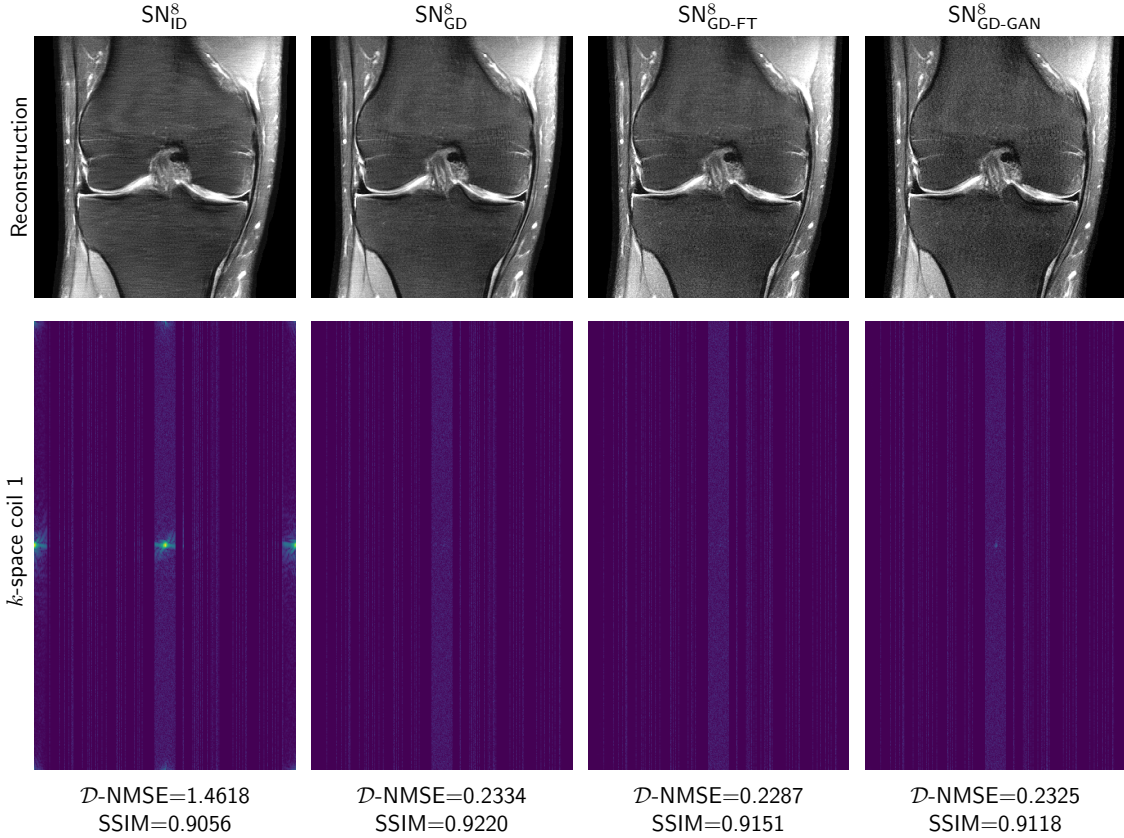
Supporting Figure 1: Examples of the heterogeneous fastMRI (51) training and validation set for coronal knee scans. The data have different number of PE lines according to the acquisition.



Supporting Figure 2: Comparison of fully-sampled RSS reconstruction (left), which is the reference of the fastMRI challenge, and the fully-sampled sensitivity-combined reconstruction (SENSE) (right). The SSIM between the two fully sampled scan is 0.6979, respectively. Although only foreground information is important, the background is also included in evaluation and has, however, a huge influence on the quantitative scores. Removing the background in both RSS and SENSE already yields an substantial increase of the SSIM to 0.9625.

Supporting Table 1: Comparison of the number of parameters for U-net and DUN. The number of parameters for one cascades equals the number of parameters for arbitrary cascades and shared parameters. The U-net and DUN have approximately the same model capacity. The model capacity for SNs and PCNs are also comparable.

Network	Regularizer	Cascades	Number of parameters
SN	UNET	1	13,424,898
SN	DUN	1	13,479,768
SN	DUN	8	107,838,144
PCN	DUN	1	13,520,117
PCN	DUN	8	108,160,936



Supporting Figure 3: `multicoil_val/file1000206.h5` slice 24  $R=4$ : This figure depicts reconstruction results for different network architectures along with the dataterm argument  $Ax - y$  of a selected coil. We observe huge deviations in  $k$ -space for  $\text{SN}^8_{\text{ID}}$ . The  $k$ -space for  $\text{SN}^8_{\text{GD}}$  and  $\text{SN}^8_{\text{GD-FT}}$  appear similar. The  $\mathcal{D}$ -NMSE is lowest for  $\text{SN}^8_{\text{GD-FT}}$ , indicating that the reconstruction adapted to the new  $k$ -space data. Although the  $\mathcal{D}$ -NMSE is lower for  $\text{SN}^8_{\text{GD-GAN}}$  than for  $\text{SN}^8_{\text{GD}}$  we observe a subtle, bright spot in the center of  $k$ -space of  $\text{SN}^8_{\text{GD-GAN}}$ , which might indicate a deviation from the ground truth for this particular slice. Note that despite better texture, the drop in SSIM of  $\text{SN}^8_{\text{GD-FT}}$  from  $\text{SN}^8_{\text{GD}}$  is expected, and is consistent with Equation [6].